

Coherent ground-state transport of neutral atoms


X. X. Li,¹ J. B. You,² X. Q. Shao^{1,3,*} and Weibin Li⁴

¹Center for Quantum Sciences and School of Physics, Northeast Normal University, Changchun 130024, China

²Institute of High Performance Computing, A*STAR (Agency for Science, Technology and Research),
1 Fusionopolis Way, Connexis, Singapore 138632

³Center for Advanced Optoelectronic Functional Materials Research,
and Key Laboratory for UV Light-Emitting Materials and Technology of Ministry of Education,
Northeast Normal University, Changchun 130024, China

⁴School of Physics and Astronomy, The University of Nottingham, Nottingham NG7 2RD, United Kingdom

 (Received 14 June 2021; revised 30 September 2021; accepted 23 February 2022; published 8 March 2022)

Quantum state transport is an important way to study the energy or information flow. By combining the unconventional Rydberg pumping mechanism and the diagonal form of van der Waals interactions, we construct a theoretical model via second-order perturbation theory to realize a long-range coherent transport inside the ground-state manifold of neutral atoms systems. With the adjustment of the Rabi frequencies and the interatomic distance, this model can be used to simulate various single-body physics phenomena such as a Heisenberg XX spin chain restricted in the single-excitation manifold, coherently perfect quantum state transfer, the parameter-adjustable Su-Schrieffer-Heeger model, and chiral motion of atomic excitation in a triangle by varying the geometrical arrangement of the three atoms, which effectively avoids the influence of atomic spontaneous emission at the same time. Moreover, the influence of atomic position fluctuation on the fidelity of quantum state transmission is discussed in detail, and the corresponding numerical results show that our work provides a robust and easily implemented scheme for quantum state transport with neutral atoms.

DOI: [10.1103/PhysRevA.105.032417](https://doi.org/10.1103/PhysRevA.105.032417)

I. INTRODUCTION

Quantum state transport plays an important role in understanding the energy or information flow at the microscopic particle level. Because of its simplicity, spin-chain systems with nearest-neighbor hopping have been extensively used to realize quantum state transmission [1–10]. To achieve high-fidelity transfer of quantum information, various transport protocols have been put forward, such as modulation of the couplings between neighboring spins [11–16], exploitation of the chiral topological edge states [17,18], and construction of a stimulated Raman adiabatic passage [19–21], especially combined with the topologically protected edge states [22,23]. Among many physical systems, Rydberg atoms have been regarded as good candidates to simulate spin-chain models on account of their remarkable properties [24–30]. In particular, the long-range interactions are capable of causing diverse consequences such as Rydberg blockade [31–33] and antiblockade [34–38] over long-range molecules [39,40].

Recently quantum state transfer schemes based on Rydberg atoms have made rapid progress both theoretically and experimentally [41–52]. According to different coding modes of qubits, these schemes can be divided into three categories: One is the spin-exchange between Rydberg states [41–44]; for instance, Barredo *et al.* [41] studied this hopping in a spin chain constructed by individually addressable

Rydberg atoms by utilizing long-range resonant dipole-dipole coupling. The second category is the quantum state transfer between the ground state and Rydberg state which remains as a second-order process in terms of laser-spin coupling [45–48]. To reach this target, Yang *et al.* [47] constructed an exchange interaction between the ground state and Rydberg state, mediated by synthetic spin exchange arising from the diagonal van der Waals (vdW) interaction. The last category is the excitation transport taking place in the ground-state manifold through a fourth-order process [49–51], where the effective spin-spin interactions between ground-state atoms are obtained by dressing Rydberg states with dipole-dipole interactions, vdW interactions, and Förster-resonance interactions.

In this work, we make use of the diagonal vdW interactions and unconventional Rydberg pumping [53,54] to realize coherent excitation transport inside the ground-state manifold of a series of three-level Rydberg atoms. The simple energy-level structure can help reduce the complexity of the experiment operation. Because the evolution dynamics of the whole system is a second-order process, we can easily modulate the effective coupling strength between adjacent sites. Consequently, the current system can be used to simulate various single-body physics phenomena such as a Heisenberg XX spin chain restricted in the single-excitation manifold [55–57], coherently perfect quantum state transfer, and the parameter-adjustable Su-Schrieffer-Heeger (SSH) model [58–60] by rearrangement of the atoms. The advantage of our system is that no fine tuning of atomic position is required because the deviation from the unconventional Rydberg pumping condition will only alter

*shaoxq644@nenu.edu.cn

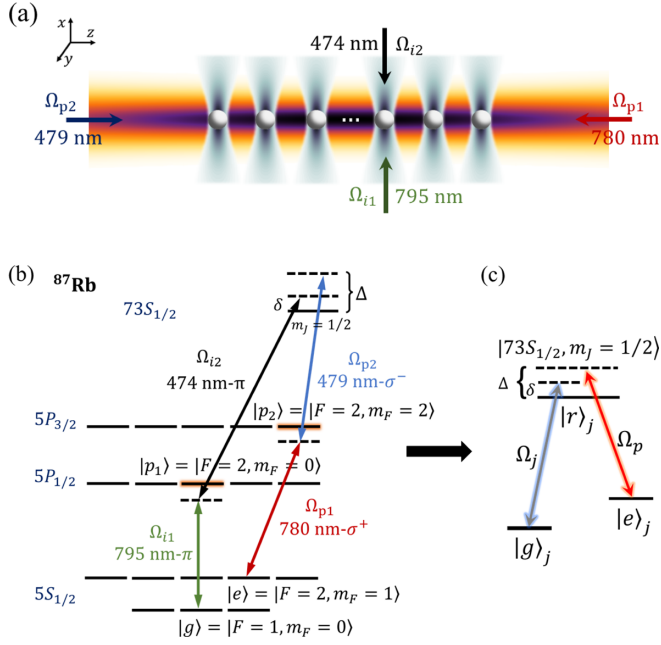


FIG. 1. Experimental setup. (a) N Rydberg atoms arranged as a linear chain at equal intervals with same energy-level configuration. Atoms are driven by two global laser fields propagating along the z axis from two sides. Meanwhile, local laser fields Ω_{i1} and Ω_{i2} propagating along the x axis are focused onto individual sites. (b) Level structure for the proposed atomic system. We consider ^{87}Rb with $|g\rangle = |5S_{1/2}, F = 1, m_F = 0\rangle$, $|e\rangle = |5S_{1/2}, F = 2, m_F = 1\rangle$, and $|r\rangle = |73S_{1/2}, m_J = 1/2\rangle$. (c) The equivalent system after adiabatically eliminating the intermediate states.

the evolution period of the quantum state without destroying the realization of the scheme.

In addition, focusing on three Rydberg atoms arranged in an equilateral triangle, a chiral motion of atomic excitation can be achieved by periodically switching on and off the weak driving fields [61], where the excitation hops from site to site in a preferred direction induced by a synthetic gauge field, breaking the time-reversal symmetry. Compared with the recent experimental observation of chiral motion in a spin-orbit-coupled Rydberg system [62], our scheme does not require precise control of electric or magnetic fields.

The remainder of this paper is organized as follows: In Sec. II we introduce the details of the system and derive its effective dynamics via effective operator method. In Sec. III we provide a protocol to realize a one-dimensional SSH model by regulating the detuning of the strong driving field. In Sec. IV, the chiral motion of atomic excitation in the triangle is accomplished via Floquet driving. In Sec. V we further analyze the feasibility of our scheme by considering a realistic experimental setup from multiple perspectives. Finally, we give a conclusion in Sec. VI.

II. ONE-DIMENSIONAL CHAIN OF ATOMS

The considered system is illustrated in Fig. 1(a), it incorporates N Rydberg atoms (^{87}Rb) with the same configuration arranged as a linear chain at equal intervals. The position of the j th atom is labeled as r_j and the distance between the j th

and k th atoms is $r_{j,k} = |r_j - r_k|$. The configuration of each atom is shown in Fig. 1(b). The ground states here are chosen as $|g\rangle = |5S_{1/2}, F = 1, m_F = 0\rangle$, $|e\rangle = |5S_{1/2}, F = 2, m_F = 1\rangle$ and the Rydberg state is selected as $|r\rangle = |73S_{1/2}, m_J = 1/2\rangle$. The transition between ground states and the Rydberg state $|r\rangle$ are driven by two-photon processes, where state $|g\rangle$ is individually addressed to the intermediate state $|p_1\rangle = |5P_{1/2}, F = 2, m_F = 0\rangle$ with a π -polarized laser field Ω_{i1} at 795 nm, and then coupled to $|r\rangle$ with another local π -polarized dressing laser Ω_{i2} at 474 nm, state $|e\rangle$ is driven by two global laser fields propagating from two sides, where Ω_{p1} at 780 nm with σ^+ -polarized drives $|e\rangle$ to the intermediate state $|p_2\rangle = |5P_{3/2}, F = 2, m_F = 2\rangle$ and Ω_{p2} at 479 nm with σ^- -polarized coupled $|p_2\rangle$ to the Rydberg state $|r\rangle$ [63,64]. After adiabatically eliminating the intermediate states $|p_{1(2)}\rangle$, the configuration of each atom can be simplified as a three-level structure shown in Fig. 1(c). The ground state $|g\rangle$ is dispersively coupled to $|r\rangle$ by a laser field of effective Rabi frequency Ω_j at site j , detuning δ , while the transition between $|e\rangle$ and $|r\rangle$ is driven by a global laser field of effective Rabi frequency Ω_p , detuned by Δ . In a rotating frame with respect to $U = \exp[-i \sum_{j=1}^N (\delta |g_j\rangle \langle g_j| + \Delta |e_j\rangle \langle e_j|) t]$, the Hamiltonian of the system reads ($\hbar = 1$)

$$H_I^{(N)} = \sum_{j=1}^N \Omega_j |r_j\rangle \langle g_j| + \Omega_p |r_j\rangle \langle e_j| + \text{H.c.} + \delta |g_j\rangle \langle g_j| + \Delta |e_j\rangle \langle e_j| + \sum_{j < k} \mathcal{U}_{jk} |r_j r_k\rangle \langle r_j r_k|. \quad (1)$$

It should be noticed that, to be more intuitive, the phases caused by the wave vectors have been ignored here but will be discussed in Sec. V A. The vdW interaction between atoms in the Rydberg state spaced $r_{j,k}$ takes the form of $\mathcal{U}_{jk} = C_6/r_{j,k}^6$. The second-order nondegenerate perturbation theory gives the dispersion coefficient C_6 of the vdW interaction as about $1.416 \text{ THz } \mu\text{m}^6$ for state $|73S_{1/2}\rangle$ [65]. So the vdW interaction continuously varies from $2\pi \times 1943 \text{ MHz}$ to $2\pi \times 1.416 \text{ MHz}$ with $r_{j,j+1}$ adjusted from 3 to $10 \mu\text{m}$. Unless otherwise specified, we assume that distance between the nearest-neighbor atoms $r_{j,j+1} = 4.1 \mu\text{m}$ for the following numerical simulation, which corresponds to $\mathcal{U}_{j,j+1} \simeq 2\pi \times 300 \text{ MHz}$.

In the limit of large detuning $\Delta \gg \Omega_p$ and the unconventional Rydberg pumping condition $\mathcal{U}_{j,j+1} = \Delta$, the high-frequency oscillating terms proportional to Δ can be neglected and the computational space is reduced for an initial state $|egg \dots g\rangle$. Meanwhile, the limiting condition $\{\Omega_p, \delta\} \gg \Omega_j$ allows us to further adiabatically eliminate the Rydberg states via the effective operator method to obtain the effective dynamics of the system [66,67].

A. Two-atom case

To explain the physical mechanism of the proposed model more clearly, we take the case of $N = 2$ as an example and assume $\Omega_1 = \Omega_2 = \Omega$, then the Hamiltonian can be simplified as

$$H_I^{(2)} = \Omega_p (|er\rangle \langle rr| + |re\rangle \langle rr|) + \Omega (|re\rangle \langle ge| + |er\rangle \langle eg|) + \text{H.c.} + \delta (|eg\rangle \langle eg| + |ge\rangle \langle ge|), \quad (2)$$

if the system is initialized in the state $|eg\rangle$, where the high-frequency oscillating terms have been neglected under the condition $U_{12} = \Delta$ and $\Delta \gg \Omega_p$. After shifting the levels of states in this subspace to make the energy of ground states $|ge\rangle$ and $|eg\rangle$ become zero, the Hamiltonian can be further rewritten as $H = H_0 + V_+ + V_-$, where

$$H_0 = \Omega_p(|er\rangle\langle rr| + |re\rangle\langle rr|) + \text{H.c.} - \delta(|er\rangle\langle er| + |re\rangle\langle re| + |rr\rangle\langle rr|), \quad (3)$$

and

$$V_+ = V_-^\dagger = \Omega(|re\rangle\langle ge| + |er\rangle\langle eg|). \quad (4)$$

Here V_+ (V_-) are assumed to be perturbative terms under the condition $\Omega \ll \{\Omega_p, \delta\}$. Generally speaking, the calculation of dissipation is very complicated if the fine structure of the system is adopted, so we first make a simple assumption that the Rydberg state decays directly into $|g\rangle$ and $|e\rangle$ with the same branching ratio of the spontaneous emission rate, i.e., $L_1 = \sqrt{\gamma/2}|g_1\rangle\langle r_1|$, $L_2 = \sqrt{\gamma/2}|g_2\rangle\langle r_2|$, $L_3 = \sqrt{\gamma/2}|e_1\rangle\langle r_1|$, and $L_4 = \sqrt{\gamma/2}|e_2\rangle\langle r_2|$. Thus the evolution of the system is now governed by the Markovian master equation

$$\partial_t \rho = -i[H_I^{(2)}, \rho] + \sum_{i=1}^4 L_i \rho L_i^\dagger - \frac{1}{2}\{L_i^\dagger L_i, \rho\}. \quad (5)$$

The excited states $|er\rangle$, $|re\rangle$, and $|rr\rangle$ can be further adiabatically eliminated when the excited states are not initially populated. Under the second-order perturbation theory, the dynamics is given by the effective operators

$$H_{\text{eff}} = -\frac{1}{2}[V_- H_{\text{NH}}^{-1} V_+ + V_+ (H_{\text{NH}}^{-1})^\dagger V_-], \quad (6)$$

and

$$L_{\text{eff}}^k = L_k H_{\text{NH}}^{-1} V_+, \quad (7)$$

where $H_{\text{NH}} = H_0 - \frac{i}{2} \sum_j L_j^\dagger L_j$. Within the subspace of consideration, the effective Hamiltonian and master equation can be obtained as

$$H_{\text{eff}}^{(2)} = J_{12}(\sigma_1^+ \sigma_2^- + \sigma_1^- \sigma_2^+), \quad (8)$$

and

$$\partial_t \rho = -i[H_{\text{eff}}^{(2)}, \rho] + \sum_{i=1}^4 L_{\text{eff}}^i \rho L_{\text{eff}}^{i\dagger} - \frac{1}{2}\{L_{\text{eff}}^{i\dagger} L_{\text{eff}}^i, \rho\}, \quad (9)$$

where

$$L_{\text{eff}}^1 = \Gamma_1 |ge\rangle\langle ge| + \Gamma_2 |ge\rangle\langle eg| + \Gamma_3(|gr\rangle\langle ge| + |gr\rangle\langle eg|), \quad (10)$$

$$L_{\text{eff}}^2 = \Gamma_1 |eg\rangle\langle eg| + \Gamma_2 |eg\rangle\langle ge| + \Gamma_3(|rg\rangle\langle ge| + |rg\rangle\langle eg|), \quad (11)$$

$$L_{\text{eff}}^3 = \Gamma_1 |ee\rangle\langle ge| + \Gamma_2 |ee\rangle\langle eg| + \Gamma_3(|er\rangle\langle ge| + |er\rangle\langle eg|), \quad (12)$$

$$L_{\text{eff}}^4 = \Gamma_1 |ee\rangle\langle eg| + \Gamma_2 |ee\rangle\langle ge| + \Gamma_3(|re\rangle\langle ge| + |re\rangle\langle eg|), \quad (13)$$

in which σ_j^+ is a pseudospin operator reading as $\sigma_j^+ = |e_j\rangle\langle g_j|$, while $J_{12} = \Omega^2 \Omega_p^2 / (\delta^3 - 2\delta \Omega_p^2)$ describes the effective coupling between ground states, $\Gamma_1 = i\Omega\chi(\gamma^2 -$

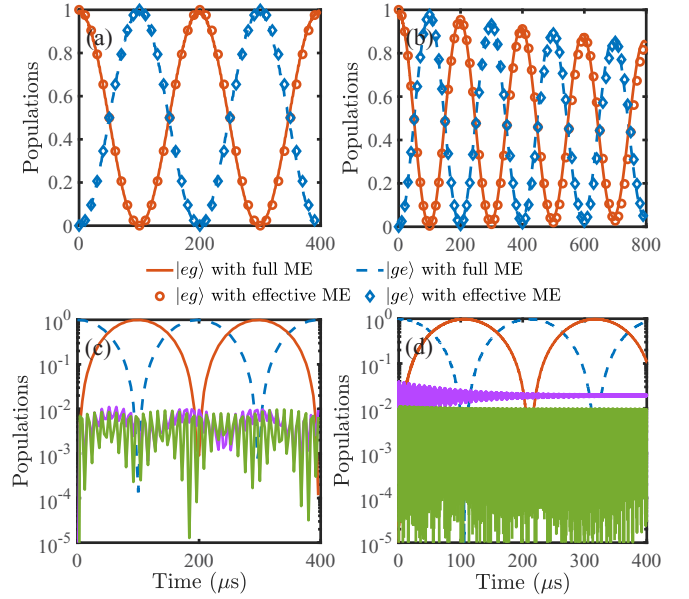


FIG. 2. (a) Populations of the two-atom states $|eg\rangle$ (solid) and $|ge\rangle$ (dashed) governed by the full Hamiltonian of Eq. (1) and the effective Hamiltonian of Eq. (8), respectively. (b) Population evolutions dominated by the full master equation (5) and effective master equation (9) with $\gamma = 2\pi \times 0.005$ MHz, respectively. (c) Populations of states $|eg\rangle$ and $|ge\rangle$ together with the singly (purple) and doubly (green) excited states governed by the full Hamiltonian of Eq. (1), where “excited state” refers to the Rydberg state $|r\rangle$. The other parameters are taken as $\delta = \Omega_p = 2\pi \times 1$ MHz, $\Omega = 0.05\Omega_p$, and $\Delta = 300\Omega_p$. (d) Populations of states $|eg\rangle$ and $|ge\rangle$ together with the singly (purple) and doubly (green) excited-states under the protocol in Ref. [49] with parameters $\Delta_s = \Delta_p = 50$ MHz, $\Omega_s = \Omega_p = 7$ MHz, and $U = 92.5$ MHz.

$3i\gamma\delta - 2\delta^2 + 2\Omega_p^2)/(\gamma - 2i\delta)$, $\Gamma_2 = -2i\Omega\Omega_p^2\chi/(\gamma - 2i\delta)$, and $\Gamma_3 = \Omega\Omega_p\chi$ are effective spontaneous emission rates with $\chi = \sqrt{2\gamma}/(\gamma^2 - 3i\gamma\delta - 2\delta^2 + 4\Omega_p^2)$. The term $[\Omega_1\Omega_2(\delta^2 - \Omega_p^2)/(\delta^3 - 2\delta\Omega_p^2) + \delta](|eg\rangle\langle eg| + |ge\rangle\langle ge|)$ appearing in the effective Hamiltonian has been disregarded because it only acts as a unit operator in the subspace we consider.

B. Numerical simulations

The resulting population oscillation between states $|eg\rangle$ and $|ge\rangle$ can be clearly seen in Fig. 2(a) without considering the dissipative parts under parameters $\delta = \Omega_p = 2\pi \times 1$ MHz, $\Omega = 0.05\Omega_p$, and $\Delta = 300\Omega_p$. The evolution governed by the effective Hamiltonian of Eq. (8) is well consistent with the full one of Eq. (1). Figure 2(b) shows the evolution dominated by the full master equation (5) and effective master equation (9) with $\gamma = 2\pi \times 0.005$ MHz, respectively. The dynamics are identical to each other, illustrating that the system can still be well described by a two-level form. To be more realistic, we introduce an uncoupled state $|\alpha\rangle$ to represent the leakage levels outside qubit basis $\{|g\rangle, |e\rangle\}$, the decay term now reads

$$\mathcal{L} = \sum_{n=1}^2 \sum_{j=g,e,\alpha} L_j^{(n)} \rho L_j^{(n)\dagger} - \frac{1}{2} L_j^{(n)\dagger} L_j^{(n)} \rho - \frac{1}{2} \rho L_j^{(n)\dagger} L_j^{(n)}, \quad (14)$$

with $L_j^{(n)} = \sqrt{b_{jr}\gamma_r}|j_n\rangle\langle r_n|$, where γ_r is the decay rate of the Rydberg state and b_{jr} denotes the branching ratios to the lower level $|j\rangle$. The transmission efficiency corresponding to the first Rabi oscillation can be denoted $T = \text{Tr}[\rho(t)I_1 \otimes |e_2\rangle\langle e_2|]$, where $t = \delta\pi/2\Omega^2$, and I is the unit operator. Without dissipation, the excitation can be transported perfectly to the second atom, and hence $T = 1$ for an ideal Heisenberg XX spin-chain model. In the presence of dissipation, we use T^λ to denote the transmission efficiency with different branching ratio $\lambda = b_{gr} + b_{er}$. In the hyperfine structure, by assuming that the dissipation rates from the Rydberg state to any ground state are equal to each other, we have $b_{gr} = 1/8$, $b_{er} = 1/8$, and $b_{or} = 3/4$ [68]. The corresponding transmission efficiency is calculated as $T^{0.25} = 0.9736$. With the pessimistic approximation that $b_{gr} + b_{er} = 0$, $b_{or} = 1$, we still have $T^0 = 0.9716$, which proves that the spontaneous radiation out of space has little effect on the system. In Figs. 2(c) and 2(d), we further compare our scheme with the method provided in Ref. [49], where the populations of singly (purple) and doubly (green) excited states (where ‘‘excited state’’ refers to the Rydberg state $|r\rangle$) are simulated by the full Hamiltonian (1) and the Hamiltonian (4) in Ref. [49], respectively. Under the condition of realizing the same Rabi oscillation period between $|eg\rangle$ and $|ge\rangle$, it can be clearly seen that our scheme has a better effect on inhibiting atomic excitation. In addition, this diatomic model can also be used to implement the $\sqrt{\text{SWAP}}$ gate which, together with single-qubit rotations, form a set of universal gates for quantum computation [69–73] (please see Appendix A for details).

Since the long-range vdW interaction between the next-nearest neighbor atoms is too weak to fulfill the condition $\Delta = \mathcal{U}_{i,i+2}$, these terms can be neglected as high-frequency oscillating terms with detuning $\Delta - \mathcal{U}_{i,i+2}$. The effective Hamiltonian for arbitrary N particles reduces to

$$H_{\text{eff}}^{(N)} = \sum_{j=1}^{N-1} J_{j,j+1} (\sigma_j^+ \sigma_{j+1}^- + \sigma_j^- \sigma_{j+1}^+), \quad (15)$$

where $J_{j,j+1} = \Omega_j \Omega_{j+1} \Omega_p^2 / (\delta^3 - 2\delta\Omega_p^2)$. Note that, when Ω_p and δ are the same magnitude, the form of the coupling strength between ground states is simplified as $-\Omega_j \Omega_{j+1} / \delta$ which is only related to the properties of the weak driving fields. As $J_{j,j+1} = J$, Eq. (15) is equivalent to a Heisenberg XX spin chain restricted in the single-excitation manifold. Figure 3(a) depicts the spin-chain dynamics of five particles governed by the full Hamiltonian of Eq. (1) from the initial state $|egggg\rangle$. The corresponding parameters are taken as $\delta = \Omega_p = 2\pi \times 1$ MHz, $\Delta = 2\pi \times 300$ MHz, and $\Omega_j = 0.05\Omega_p$. Meanwhile, the perfect quantum state transfer can be also achieved by tuning the Rabi frequencies Ω_j to meet the condition $J_{j,j+1} = J\sqrt{j(N-j)}$ [11]. For five particles, the corresponding parameters can be selected as $\Omega_1 = \Omega_5 = \Omega$, $\Omega_2 = \Omega_4 = 2\Omega$, and $\Omega_3 = \sqrt{3}/2\Omega$, where $\Omega = 0.025\Omega_p$. The populations of single-excited states under the full Hamiltonian of Eq. (1) are shown in Fig. 3(b).

Experimentally, there may be a systematic error in the position of atoms destroying the condition $\mathcal{U}_{j,j+1} = \Delta$. To investigate the influence of this factor, we introduce the degree of deviation $\Delta U = \mathcal{U}_{j,j+1} - \Delta$. To ensure that the near-

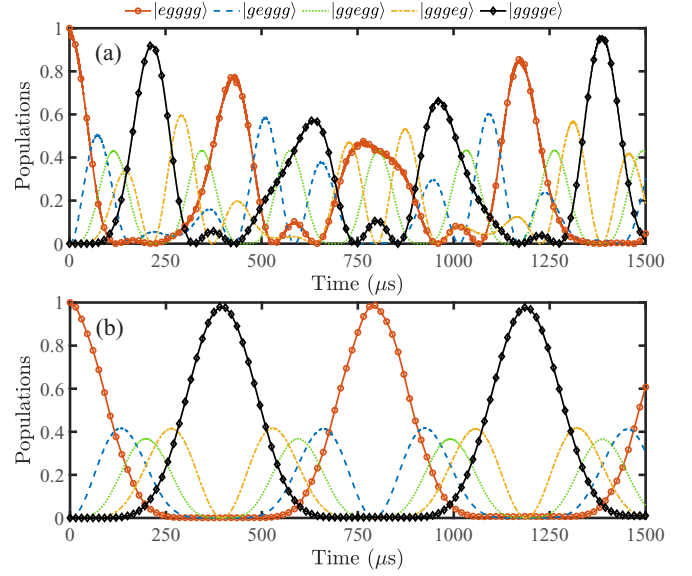


FIG. 3. Transport dynamics of the multi-atomic model with $N = 5$ without considering spontaneous emission. (a) Populations of ground states with same separation and coupling strength governed by the full Hamiltonian of Eq. (1) with $\Omega_j = 0.05\Omega_p$. (b) The evolution of ground states governed by the full Hamiltonian under the perfect transmission condition $\Omega_1 = \Omega_5 = \Omega$, $\Omega_2 = \Omega_4 = 2\Omega$, $\Omega_3 = \sqrt{3}/2\Omega$ with $\Omega = 0.025\Omega_p$, while the other parameters are taken as $\Omega_p = 2\pi \times 1$ MHz, $\delta = \Omega_p$, and $\mathcal{U}_{i,i+1} = \Delta = 2\pi \times 300$ MHz.

resonance terms kept before are still dominant, we assume that ΔU is not very large. After calculation by the effective operator method, the effective Hamiltonian keeps the same form as Eq. (8) but with an updated coupling strength related to ΔU :

$$J_{12} = \frac{\Omega^2 \Omega_p^2}{\delta^3 - 2\delta\Omega_p^2 - \delta^2 \Delta U}. \quad (16)$$

Setting $\delta = \Omega_p = 2\pi \times 1$ MHz, $\Delta = 2\pi \times 300$ MHz, and $\Omega = 0.05\Omega_p$, the dynamical evolution modeled by different ΔU is shown in Fig. 4. With such parameters, we have $\delta^3 - 2\delta\Omega_p^2 < 0$. According to Eq. (16), when $\Delta U > 0$, the increased value of $|\Delta U|$ will lead to the decrease of the coupling coefficient J_{12} and the extension of the evolution period. When $\Delta U < 0$, the evolution period is shortened under the condition $0 < |\Delta U| < (1 + 2\delta\Omega_p^2 - \delta^3)/\delta^2$ and extended under the condition $|\Delta U| > (1 + 2\delta\Omega_p^2 - \delta^3)/\delta^2$. Note that $\Delta U = -(1 + 2\delta\Omega_p^2 - \delta^3)/\delta^2$ is a singularity of Eq. (16), which will destroy the condition of second-order perturbation and should be avoided when considering the actual physical parameters. On the whole, in the presence of a small deviation, the above derivation process is still valid and the effective coupling strength $J_{j,j+1}$ becomes a function of ΔU which will only change the evolution cycle of the system but will not invalidate the scheme. Here, we only consider the case where the atomic position is fixed for simplicity; the random fluctuation of vdW interaction caused by the atomic vibration will be further discussed in Sec. VB.

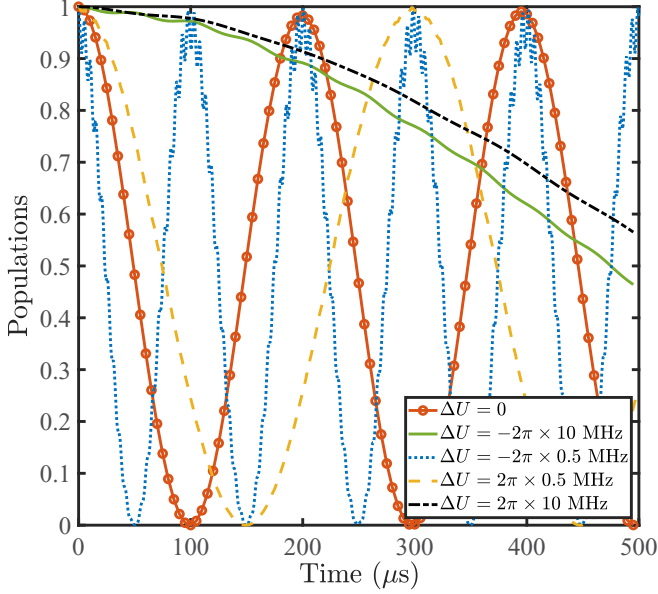


FIG. 4. The mismatch of the unconventional Rydberg pumping condition governed by full Hamiltonian (1). The parameters are taken as $\delta = \Omega_p = 2\pi \times 1$ MHz, $\Delta = 2\pi \times 300$ MHz, $\Omega = 0.05\Omega_p$, and $\Delta U = U_{j,j+1} - \Delta$.

III. TOPOLOGICAL SPIN MODEL

Inspired by the inherent adjustable coupling of the system, we show that the following one-dimensional (1D) SSH model can be constructed [58–60,74–77]

$$H_{\text{ssh}} = \sum_{i=1}^{\frac{N}{2}} J_a \sigma_{2i-1}^+ \sigma_{2i}^- + \sum_{i=1}^{\frac{N}{2}-1} J_b \sigma_{2i}^+ \sigma_{2i+1}^- + \text{H.c.}, \quad (17)$$

with regard to even number of particles, where J_a and J_b represent real intra- and interunit-cell hopping coefficients, respectively. Different from the previous scheme (i.e., $U = \Delta$), we here take the deviation of the unconventional Rydberg pumping condition ΔU as a control parameter to achieve our goal. When $U_{j,j+1}$ is significantly different from Δ (ΔU is relatively large), the extra coupling induced by doubly “excited” states with two atoms in state $|e\rangle$ while others in $|g\rangle$ should also be taken into account. For the simplest system composed of three particles with nonidentical coupling, the transition paths are shown in Fig. 5(a). Thus the form of H_{NH} and V_+ should be rewritten as

$$\begin{aligned} H_{\text{NH}} = & (\Delta U_a - \delta) |rrg\rangle\langle rrg| - \delta(|erg\rangle\langle erg| + |reg\rangle\langle reg| \\ & + |ger\rangle\langle ger| + |gre\rangle\langle gre|) + (\Delta U_b - \delta) |grr\rangle\langle grr| \\ & + (\Delta - \delta)(|eeg\rangle\langle eeg| + |gee\rangle\langle gee|) \\ & + \Omega_p(|ger\rangle\langle grr| + |gre\rangle\langle grr| + |ger\rangle\langle gee| \\ & + |gre\rangle\langle gee| + |erg\rangle\langle rrg| + |reg\rangle\langle rrg| \\ & + |erg\rangle\langle eeg| + |reg\rangle\langle eeg| + \text{H.c.}), \end{aligned} \quad (18)$$

and

$$\begin{aligned} V_+ = & \Omega_2 |erg\rangle\langle eeg| + \Omega_1 |reg\rangle\langle geg| + \Omega_3 |ger\rangle\langle geg| \\ & + \Omega_2 |gre\rangle\langle gge|, \end{aligned} \quad (19)$$

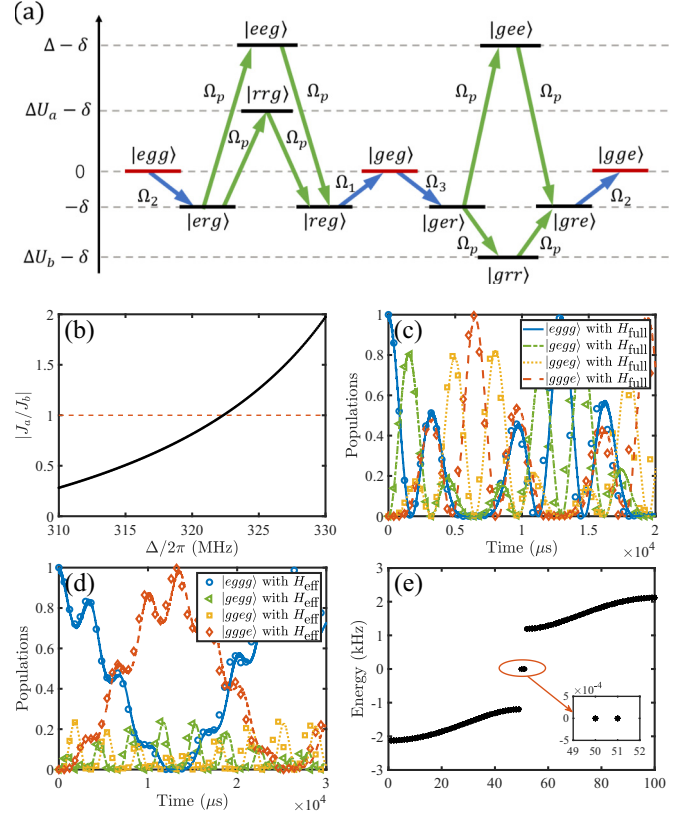


FIG. 5. (a) The effective coupling processes for topological spin model. (b) The ratio of J_a to J_b is shown as a function of detuning Δ . (c) Populations of ground states $|eggg\rangle$ (solid), $|gegg\rangle$ (dot-dashed), $|ggeg\rangle$ (dotted), and $|ggge\rangle$ (dashed) governed by full and effective Hamiltonian shown as Eqs. (1) and (17) with $\Delta = 2\pi \times 330$ MHz. (d) The population evolutions of ground states with $\Delta = 2\pi \times 310$ MHz. (e) The energy spectrum with topological phase with $N = 100$, where $\Delta = 2\pi \times 310$ MHz. The other parameters are taken as $\delta = \Omega_p = 2\pi \times 1$ MHz, $\Omega_j = 0.05\Omega_p$, $r_{2i-1,2i} = 4 \mu\text{m}$, and $r_{2i,2i+1} = 4.1 \mu\text{m}$.

where $\Delta U_k = U_k - \Delta$, $k = a, b$, $U_a \propto 1/r_{2i-1,2i}^6$, and $U_b \propto 1/r_{2i,2i+1}^6$. Assuming $\Omega_j = \Omega$ and applying the effective operator method again, the Rydberg states can be adiabatically eliminated and the effective coupling strength between ground states can be obtained as

$$J_k = -\frac{\Omega^2 \Omega_p^2 (U_k - \delta)}{\delta^4 - U_k \delta^3 - \eta_k \delta^2 + 2U_k \Omega_p^2 \delta}, \quad (20)$$

where $\eta_k = 4\Omega_p^2 + \Delta^2 - U_k \Delta$. If the two distances between atoms are set to be $r_{2i-1,2i} = 4 \mu\text{m}$ and $r_{2i,2i+1} = 4.1 \mu\text{m}$, the corresponding vdW interactions are $U_a \simeq 2\pi \times 346$ MHz and $U_b \simeq 2\pi \times 300$ MHz. Therefore, after setting other parameters as $\delta = \Omega_p = 2\pi \times 1$ MHz and $\Omega = 0.05\Omega_p$, the effective coupling strength J_k becomes a single-valued function of Δ . As illustrated in Fig. 5(b), the ratio $|J_a/J_b|$ is related to the topological phase. When $\Delta \in 2\pi \times [310, 323]$ MHz, the system corresponds to a nontrivial topological phase for $|J_a/J_b| < 1$, where an additional state localized at the boundaries around zero energy can be observed. When $\Delta \in 2\pi \times [323, 330]$ MHz, the system corresponds to a trivial phase for $|J_a/J_b| > 1$ with two discrete energy bands. So

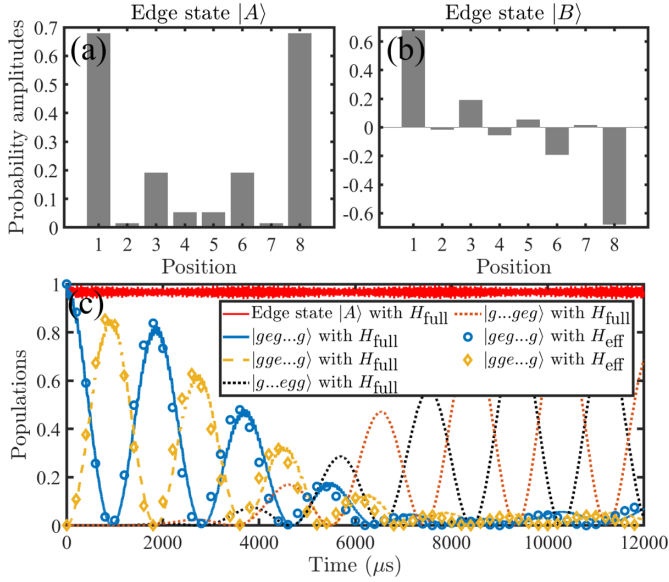


FIG. 6. The transport dynamics and the edge states of the system with $N = 8$. Panels (a) and (b) correspond to the probability amplitudes of two edge states governed by the effective Hamiltonian (17). (c) Populations of the edge state $|A\rangle$ governed by the full Hamiltonian (1) (solid line) and the populations of states $|geg \dots g\rangle$ and $|gge \dots g\rangle$ governed by the full (dashed and dotted) and effective (diamonds and circles) Hamiltonian initially excited at the second particle, respectively. The parameters are $\delta = \Omega_p = 2\pi \times 1$ MHz, $\Omega = 0.05\Omega_p$, $\Delta = 2\pi \times 310$ MHz, $r_{2i-1,2i} = 4 \mu\text{m}$, and $r_{2i,2i+1} = 4.1 \mu\text{m}$.

the system can be modulated from the nontrivial topological phase to trivial topological phase by regulating the detuning Δ from $2\pi \times 310$ MHz to $2\pi \times 330$ MHz within the current parameter setting range. Figures 5(c) and 5(d) respectively show the evolution of ground states of $N = 4$ with $\Delta = 2\pi \times 330$ MHz and $\Delta = 2\pi \times 310$ MHz. The evolution governed by the effective Hamiltonian (17) is well consistent with the full Hamiltonian (1), which proves that the approximation is valid. In Fig. 5(e), we characterize the energy spectrum of a multiparticle ($N = 100$) SSH model in the case of a single excitation with $\Delta = 2\pi \times 310$ MHz. The gap between the edge state and bulk is about 1.2 kHz, which corresponds to a nontrivial topological phase with two zero-energy edge states.

Figure 6 further reveals the edge states and the transport dynamics of the system with eight particles. Figures 6(a) and 6(b) correspond to the probability amplitudes of two edge states governed by the effective Hamiltonian, which are mainly distributed on two sides. Figure 6(c) shows the evolution results for two different initial conditions, the edge state $|A\rangle$ and $|gegg \dots\rangle$. The edge state $|A\rangle$ does not transfer to other states and oscillates around 1, but the population of state $|geg \dots g\rangle$ transfers to the intermediate particles except the two sides. This behavior characterizes as the topological structure. We can also see from Fig. 6 that the dynamics described by the effective Hamiltonian (marked with a circle and diamond) is the same as the full Hamiltonian. Therefore, using the ground state of Rydberg atom can construct an effective SSH model and help to further provide an alternative way for realization of quantum state transmission based on topological model [22,23].

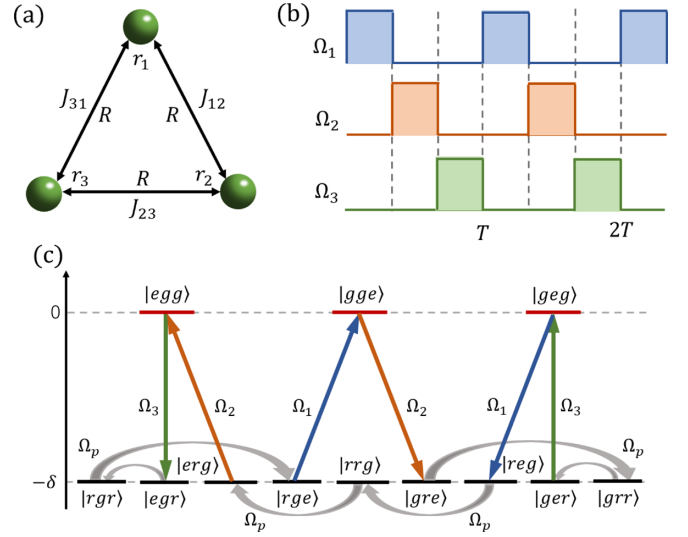


FIG. 7. (a) Schematic representations of Rydberg atoms arranged as an equilateral triangle form, J_{jk} describes the effective coupling between the j th and k th atoms. (b) Periodic modulated pulses for realizing the chiral motion of atomic excitation. (c) The effective coupling processes have been chosen for realizing the chiral motion.

IV. CHIRAL MOTION OF ATOMIC EXCITATION

Compared with the tight-binding model with open boundary conditions, the tight-binding model with periodic boundary conditions can exhibit more abundant physical properties. For three particles arranged in an equilateral triangle shown in Fig. 7(a), the following form of Hamiltonian can exist under the induction of a gauge field:

$$H_{\Phi_z} = -J_c (e^{i\phi_{12}} \sigma_1^+ \sigma_2^- + e^{i\phi_{23}} \sigma_2^+ \sigma_3^- + e^{i\phi_{31}} \sigma_3^+ \sigma_1^-) + \text{H.c.}, \quad (21)$$

where J_c is a positive real number and $\Phi_z = \phi_{12} + \phi_{23} + \phi_{31}$ can be seen as a synthetic flux behaving similarly to a physical magnetic flux. When $\Phi_z = \pi/2$, the atomic excitation $|e\rangle$ propagates in the counterclockwise direction $1 \rightarrow 3 \rightarrow 2 \rightarrow 1$. When $\Phi_z = -\pi/2$, the direction of transmission reverses. Ever the synthetic flux $\Phi_z \neq 0$, the dynamics of the system breaks the time-reversal symmetry known as chiral motion [61,62].

In our scheme, this chiral motion can be simulated by periodic modulation under the Floquet theorem [78–83], and the phase of the hopping amplitude between adjacent sites can be induced through the noncommutativity between Hamiltonians. To be specific, the piecewise constant Hamiltonian is shown in the form of

$$H(t) = \begin{cases} H_1, & t \in [0, T/3) \\ H_2, & t \in [T/3, 2T/3) \\ H_3, & t \in [2T/3, T), \end{cases} \quad (22)$$

where

$$H_i = \Omega_i |r_i\rangle \langle g_i| + \sum_{j=1}^3 \Omega_{pj} |r_j\rangle \langle e_j| + \text{H.c.} + \delta |g_j\rangle \langle g_j| + \Delta |e_j\rangle \langle e_j| + \sum_{j<k} \mathcal{U}_{jk} |r_j r_k\rangle \langle r_j r_k|. \quad (23)$$

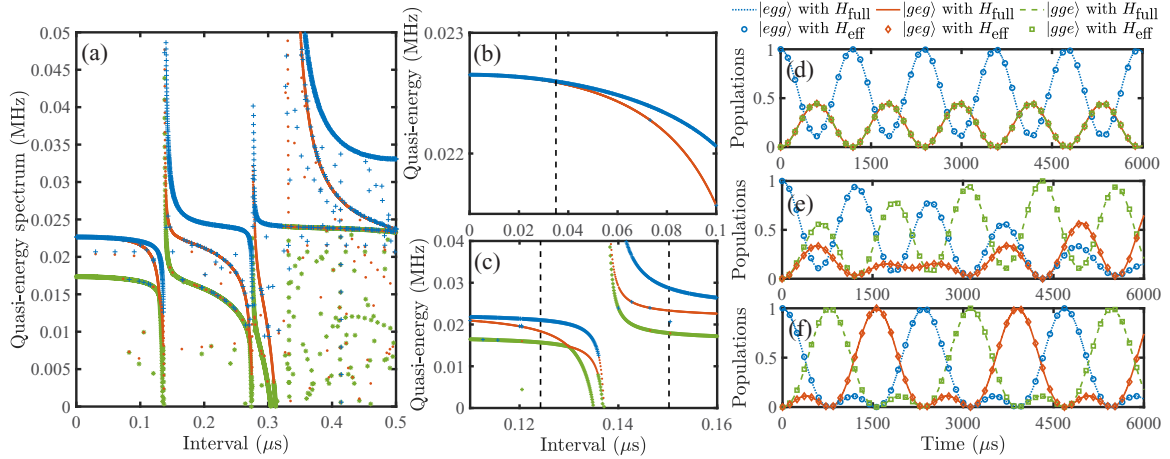


FIG. 8. (a) The quasienergy spectrum of the effective Hamiltonian $H_{\text{eff}} = i \ln(e^{-iH_3\tau} e^{-iH_2\tau} e^{-iH_1\tau})/3\tau$ under various time intervals τ . Panels (b) and (c) show the enlarged view of the quasienergy spectrum, which respectively show the energy-splitting process and the position the chiral motion generated. Panels (d)–(f) show the populations of the ground states under different time intervals, respectively corresponding to the quasienergy spectrum with two degenerate eigenenergies, arbitrary split three eigenenergies, and the eigenenergy with the same separations, where $\tau = 0.01 \mu\text{s}$, $0.1 \mu\text{s}$, and $0.12425 \mu\text{s}$. The parameters are $\delta = \Omega_p = 2\pi \times 1 \text{ MHz}$, $\Omega = 0.05\Omega_p$, and $\Delta = 2\pi \times 300 \text{ MHz}$.

In this case, the evolution period of the system has been set to T , it contains three processes and each one is described by H_i corresponding to the evolution time $\tau = T/3$. This can be achieved by switching on and off the weak fields coupled to the transition between states $|g\rangle$ and $|r\rangle$ of atoms in sequence. Considering the effect of all 27 states on the system dynamics during alternation, the effective Hamiltonian is presented as $H_{\text{eff}} = i \ln(e^{-iH_3\tau} e^{-iH_2\tau} e^{-iH_1\tau})/T$ [84]. The quasienergy spectrum of this effective Hamiltonian under various time intervals is displayed in Fig. 8(a), keeping only the eigenenergies in the ground-state manifold constructed by $|egg\rangle$, $|geg\rangle$, and $|gge\rangle$ for the sake of clarity. When in the time interval $\tau < 0.035 \mu\text{s}$, there exists a double-degenerate quasienergy spectrum and the effective Hamiltonian can be well described by the Trotter product formula $\lim_{N \rightarrow \infty} \{e^{-iH_3T/3N} e^{-iH_2T/3N} e^{-iH_1T/3N}\}^N = e^{-i(H_1+H_2+H_3)T/3}$ [85,86], then we have $H_{\text{eff}} = \sum_{j=1}^3 J'_{j,j+1} (\sigma_j^+ \sigma_{j+1}^- + \sigma_j^- \sigma_{j+1}^+)$, where $J'_{j,j+1} = \Omega_j \Omega_{j+1} \Omega_p^2 / 9(\delta^3 - 2\delta\Omega_p^2)$ ($\Omega_4 = \Omega_1$). This condition is identical to the population evolution of ground states with $\tau = 0.01 \mu\text{s}$ shown in Fig. 8(d). Due to the influence of the hopping phase, the degeneracy is removed as τ gets longer and the population evolution is shown in Fig. 8(e) with $\tau = 0.1 \mu\text{s}$. When the difference between the eigenenergies is equal as indicated in Fig. 8(c), the phase induced by the alternate evolution is just $\pm\pi/2$, resulting in a directional chiral motion of atomic excitation, as shown in Fig. 8(f) for $\tau = 0.12425 \mu\text{s}$.

A combination of numerical and analytical methods can be employed to determine the specific value of $\Phi_{12(23,31)}$ corresponding to various time intervals. According to Eq. (23), under the condition $\mathcal{U}_{j,j+1} = \Delta \gg \{\Omega_p, \delta\} \gg \Omega_i$, we can neglect the high-frequency oscillating terms and the dynamics of the system are mainly restricted in the subspace constructed by $|egg\rangle$, $|egr\rangle$, $|rgr\rangle$, $|rge\rangle$, $|gge\rangle$, $|gre\rangle$, $|grr\rangle$, $|ger\rangle$, $|geg\rangle$, $|reg\rangle$, $|rrg\rangle$, and $|erg\rangle$, as shown in Fig. 7(c). To simplify computational space, we complete the following calculations in the subspace composed of the above 12 states. Once the

interval τ is given, the effective Hamiltonian can be numerically obtained via second-order perturbation theory. Keeping the convergent results and discarding the divergent results, we have the effective Hamiltonian form as

$$H_{\text{eff}} = -J_{\text{eff}}^{12} e^{i\Phi_{12}} |egg\rangle \langle geg| - J_{\text{eff}}^{23} e^{i\Phi_{23}} |geg\rangle \langle gge| - J_{\text{eff}}^{31} e^{i\Phi_{31}} |gge\rangle \langle egg| + \text{H.c.}, \quad (24)$$

corresponding to a certain time interval τ . The average values of J_{eff} [$J_{\text{eff}} = 1/3(J_{\text{eff}}^{12} + J_{\text{eff}}^{23} + J_{\text{eff}}^{31})$] and Φ [$\Phi = 1/3(\Phi_{12} + \Phi_{23} + \Phi_{31})$] versus different time intervals are displayed in Figs. 9(a) and 9(b), respectively. From which we can read the specific value of J_{eff} and Φ for any τ . For example, when $\tau = 0.01 \mu\text{s}$, we have $J_{\text{eff}} \simeq 1.763 \text{ kHz}$, $\Phi \simeq 0$, when $\tau = 0.1 \mu\text{s}$, we have $J_{\text{eff}} \simeq 1.7 \text{ kHz}$, $\Phi \simeq 0.0263\pi$, and when $\tau = 0.12425 \mu\text{s}$, we have $J_{\text{eff}} \simeq 1.55 \text{ kHz}$, $\Phi \simeq 0.1643\pi$. The system dynamics corresponding to $\tau = \{0.01, 0.1, 0.12425\} \mu\text{s}$ governed by the effective Hamiltonian (24) with the above J_{eff} and Φ shown in Figs. 8(d)–8(f). The evolutions of populations coincide with the full one of Eq. (22), which indicates that the effective results are reliable. According to the continuity equation on the lattice [87–89],

$$\frac{d}{dt} \sigma_j^z = i[H_{\text{eff}}, \sigma_j^z] = \nabla_j I_j = I_{j,j-1} - I_{j,j+1}, \quad (25)$$

where $\sigma_j^z = |e_j\rangle \langle e_j| - |g_j\rangle \langle g_j|$, one can find that the expectation value of the current operator in the ground state of Eq. (24) for the bond $j \rightarrow j+1$ on the lattice is given by

$$\langle I_{j,j+1} \rangle = 2iJ_{\text{eff}}^{j,j+1} (e^{i\Phi_{j,j+1}} \langle \sigma_j^+ \sigma_{j+1}^- \rangle - \text{c.c.}). \quad (26)$$

Corresponding to Figs. 8(d)–8(f), the ground-state current for the bond $1 \rightarrow 2$ are measured as $\{0, -0.0596, -0.3376\} \text{ kHz}$.

When $\Phi = \pm\pi/6$, the chiral motion holding a definite direction can be successfully obtained since the effective Hamiltonian of the system fits Eq. (21). As can be seen from Fig. 9(b), multiple time intervals can be selected, and we only choose the shortest time to discuss for convenience. Figures 9(c) [9(e)] and 9(d) [9(f)] respectively show the

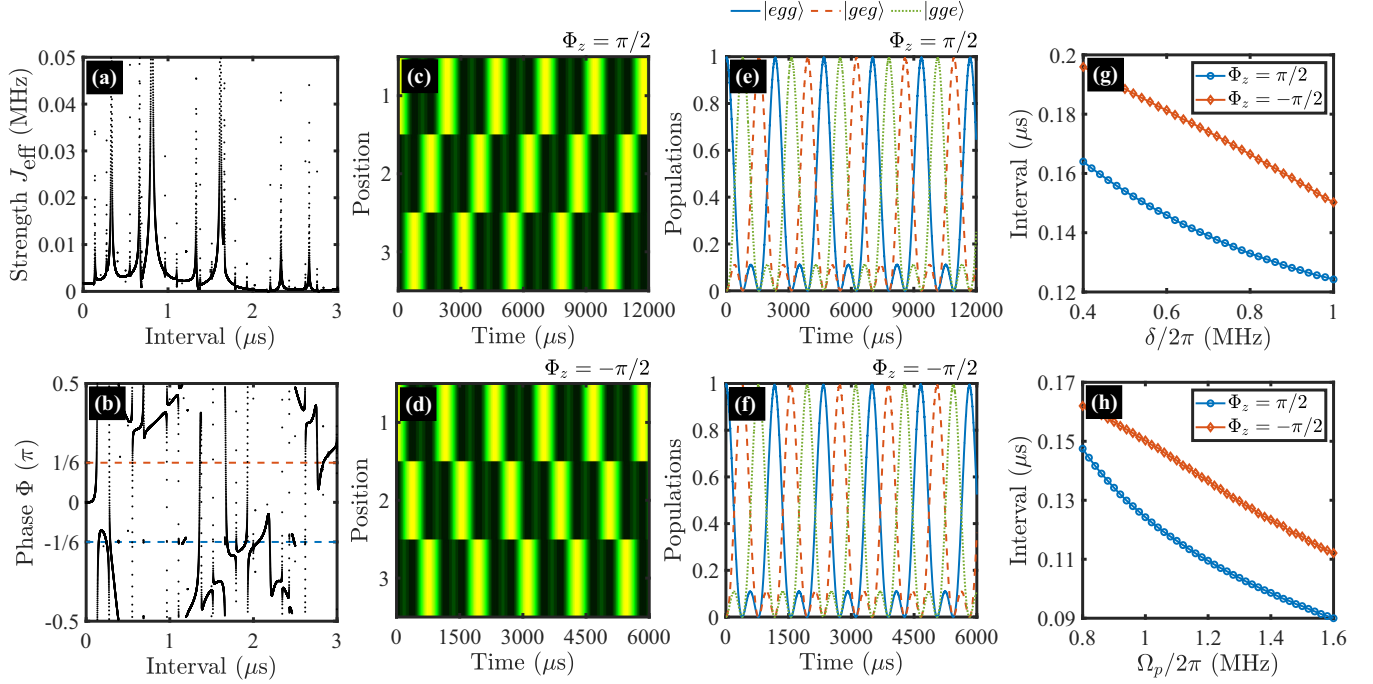


FIG. 9. The chiral motion of atomic excitation under the equilateral-triangle structure. Panels (a) and (b) respectively show the average value of the effective coupling strength and induced phases under different time intervals. Panels (c) and (d) intuitively represent the transfer of the ground state between three positions. Panels (e) and (f) further show the populations of ground states as a function of time measured for values of $\Phi_z = \pi/2, -\pi/2$ while the time interval is respectively taken as $0.12425 \mu\text{s}$ and $0.15025 \mu\text{s}$. The parameters are $\delta = \Omega_p = 2\pi \times 1 \text{ MHz}$, $\Omega_j = 0.05\Omega_p$, and $\Delta = 2\pi \times 300 \text{ MHz}$. Panels (g) and (h) show the time interval $\tilde{\tau}$ as functions of parameters δ and Ω_p , respectively.

excited population transport between different atoms governed by the full Hamiltonian (22) with $\tilde{\tau}_{ac} = 0.12425 \mu\text{s}$ and $\tilde{\tau}_c = 0.15025 \mu\text{s}$. Note that $\tilde{\tau}$ represents the time interval at which $\Phi = \pm\pi/6$ in later descriptions. From the atomic arrangement shown in Fig. 7(a), we can see that $\tilde{\tau}_{ac(c)}$ leads to the anticlockwise (clockwise) current. Thus, the direction of motion can be controlled by changing τ . The parameters have been taken as $\delta = \Omega_p = 2\pi \times 1 \text{ MHz}$, $\Omega = 0.05\Omega_p$, and $\Delta = \mathcal{U}_{j,k} = 2\pi \times 300 \text{ MHz}$, and the effective coupling strength $J_{\text{eff}}^{(2)} \simeq 1.55$ (3.14) kHz matching $\tilde{\tau}_{ac(c)}$. Since the effective coupling strength is a function of Ω_j , Ω_p , and δ , the time interval $\tilde{\tau}$ required to get this directional chiral motion is possibly related to these parameters. We have performed numerical simulations under different parameters and the comparison shows that $\tilde{\tau}$ is closely related to δ and Ω_p . With parameters $\Omega = 0.05\Omega_p$ and $\Delta = \mathcal{U}_{j,k} = 2\pi \times 300 \text{ MHz}$, Figs. 9(g) and 9(h) further characterize the change of $\tilde{\tau}$ with δ for a fixed $\Omega_p = 2\pi \times 1 \text{ MHz}$ and with Ω_p for a fixed $\delta = 2\pi \times 1 \text{ MHz}$, respectively. After polynomial fitting, we obtain $\tilde{\tau}$ as a function of δ and Ω_p , presented as $\tilde{\tau} = p_5\delta^4 + p_4\delta^3 + p_3\delta^2 + p_2\delta + p_1$ and $\tilde{\tau} = q_5\Omega_p^4 + q_4\Omega_p^3 + q_3\Omega_p^2 + q_2\Omega_p + q_1$, where the coefficients corresponding to $\Phi_z = \pm\pi/2$ are shown in Table I. Therefore, according to any $\delta \in [0.8\pi, 2\pi] \text{ MHz}$ or $\Omega_p \in [1.6\pi, 3.2\pi] \text{ MHz}$, the time interval $\tilde{\tau}$ can be estimated through the above functions.

V. DISCUSSION

Considering a realistic experimental setup, there are some problems that should be addressed by further discussions,

such as the phase induced by wave vectors, the atomic position fluctuation, and the effectiveness of the vdW interaction.

A. Phases induced by wave vectors

To be more intuitive, the phases caused by the wave vectors have been ignored in above analysis. However, once the wave vectors are specified, the corresponding phases should be taken into account.

For the method of quantum state transport, ^{87}Rb atoms are arranged in a line along the quantization z axis. The phases induced by the individual beams Ω_{i1} and Ω_{i2} can be neglected, but the global laser fields Ω_{pi} propagating along the z axis will induce phase factors $e^{ik_{pi}\cdot\mathbf{r}_i}$. Since the global laser beams are counterpropagating along the z axis, the effective wave

TABLE I. Coefficients corresponding to numerical fitting results.

$\Phi_z = \pi/2$	$\Phi_z = -\pi/2$
$p_1 = 0.23278 \text{ MHz}^{-1}$	$p_1 = 0.24661 \text{ MHz}^{-1}$
$p_2 = -4.0934 \times 10^{-2} \text{ MHz}^{-2}$	$p_2 = -3.2661 \times 10^{-2} \text{ MHz}^{-2}$
$p_3 = 7.0238 \times 10^{-3} \text{ MHz}^{-3}$	$p_3 = 7.3238 \times 10^{-3} \text{ MHz}^{-3}$
$p_4 = -7.3771 \times 10^{-4} \text{ MHz}^{-4}$	$p_4 = -1.0702 \times 10^{-3} \text{ MHz}^{-4}$
$p_5 = 3.4895 \text{ MHz}^{-5}$	$p_5 = 5.4603 \times 10^{-5} \text{ MHz}^{-5}$
$q_1 = 0.52719 \text{ MHz}^{-1}$	$q_1 = 9.0639 \times 10^{-2} \text{ MHz}^{-1}$
$q_2 = -0.16104 \text{ MHz}^{-2}$	$q_2 = 5.1437 \times 10^{-2} \text{ MHz}^{-2}$
$q_3 = 2.5016 \times 10^{-2} \text{ MHz}^{-3}$	$q_3 = -1.1041 \times 10^{-2} \text{ MHz}^{-3}$
$q_4 = -1.8631 \times 10^{-3} \text{ MHz}^{-4}$	$q_4 = 8.3451 \times 10^{-4} \text{ MHz}^{-4}$
$q_5 = 5.3498 \times 10^{-5} \text{ MHz}^{-5}$	$q_5 = -2.2295 \times 10^{-5} \text{ MHz}^{-5}$

vector introduced by Ω_p is $k_z/2\pi = |\lambda_{p1}^{-1} - \lambda_{p2}^{-1}| \simeq 5.062 \times 10^6 \text{ m}^{-1}$. Taking $N = 2$ as an example, after denoting the position of the two atoms as $\mathbf{r}_1 = (0, 0, z_1)$ and $\mathbf{r}_2 = (0, 0, z_2)$, the system Hamiltonian (1) is rewritten as

$$H_I^{(N)} = \sum_{j=1}^N \Omega_j |r_j\rangle \langle g_j| + \Omega_p e^{ik_z z_j} |r_j\rangle \langle e_j| + \text{H.c.} + \delta |g_j\rangle \langle g_j| + \Delta |e_j\rangle \langle e_j| + \sum_{j < k} U_{jk} |r_j r_k\rangle \langle r_j r_k|. \quad (27)$$

Meanwhile, the Hamiltonian shown in Eqs. (3) and (4) should be modified as

$$H_{ph} = \Omega_p (e^{ik_z z_1} |er\rangle \langle rr| + e^{ik_z z_2} |re\rangle \langle rr|) + \text{H.c.} - \delta (|er\rangle \langle er| + |re\rangle \langle re| + |rr\rangle \langle rr|), \quad (28)$$

and

$$V_+ = V_-^\dagger = \Omega_1 |re\rangle \langle ge| + \Omega_2 |er\rangle \langle eg|. \quad (29)$$

Applying the effective operator method

$$H_{\text{eff}} = -\frac{1}{2} [V_- H_{ph}^{-1} V_+ + V_+ (H_{ph}^{-1})^\dagger V_-], \quad (30)$$

we have

$$H_{\text{eff}} = J_{12} e^{ik_z(z_2 - z_1)} |ge\rangle \langle eg| + \text{H.c.}, \quad (31)$$

where $J_{12} = \Omega_1 \Omega_2 \Omega_p^2 / (\delta^3 - 2\delta \Omega_p^2)$. Starting from the initial state $|eg\rangle$, governed by the effective Hamiltonian of Eq. (31), we have $|\Psi(t)\rangle = \cos(J_{12}t) |eg\rangle - ie^{ik_z(z_2 - z_1)} \sin(J_{12}t) |ge\rangle$. The wave vector introduces an extra relative phase $e^{ik_z(z_2 - z_1)}$ between state $|eg\rangle$ and $|ge\rangle$. It is apparent from the above form that the effective phase factor caused by wave vectors is only related to the relative position of the adjacent atoms. Therefore it is easy to obtain the effective Hamiltonian for arbitrary N particles read as

$$H_{\text{eff}}^{(N)} = \sum_{j=1}^{N-1} J_{j,j+1} e^{-ik_z r} \sigma_j^+ \sigma_{j+1}^- + \text{H.c.}, \quad (32)$$

where $J_{j,j+1} = \Omega_j \Omega_{j+1} \Omega_p^2 / (\delta^3 - 2\delta \Omega_p^2)$. Starting from the initial state $\sigma_1^+ |gg \dots g\rangle_N$, extra phases $e^{i(j-1)k_z r}$ are introduced to states $\sigma_j^+ |gg \dots g\rangle_N$. However, these relative phases do not affect the transmission of the single-excited state, as shown in Figs. 10(a) and 10(b), where the system dynamics is simulated by Hamiltonian (27) for the case of $N = 2$ and 3.

From another perspective, by absorbing the phase factor $e^{-ik_z(z_{j+1} - z_j)}$ into the redefined space-dependent state $|\tilde{e}_j\rangle = e^{ik_z z_j} |e_j\rangle$, the effective Hamiltonian under the new basis vectors can be written as

$$H_{\text{eff}}^{(N)} = \sum_{j=1}^{N-1} J_{j,j+1} \tilde{\sigma}_j^+ \tilde{\sigma}_{j+1}^- + \text{H.c.}, \quad (33)$$

where $\tilde{\sigma}_j^+ = |\tilde{e}_j\rangle \langle g_j|$, which remains to a Heisenberg XX spin chain restricted in the single-excitation manifold.

For the topological model, a relative phase exists between \tilde{J}_a and \tilde{J}_b owing to various spaces between atoms, which is

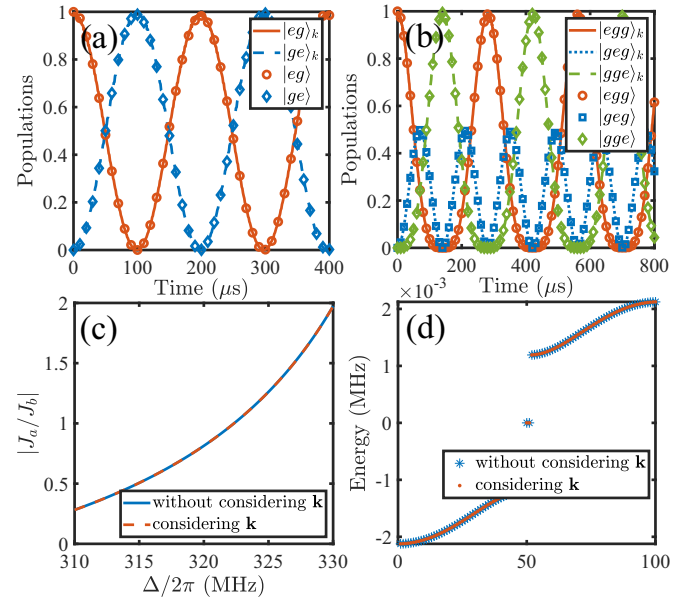


FIG. 10. The system dynamics with and without considering the wave vectors (marked with subscript k after the ket symbol). Panels (a) and (b) correspond to the dynamics of an isometric chain structure with $N = 2$ and $N = 3$, respectively, where $r = 4.1 \mu\text{m}$. The evolutions are governed by Eqs. (1) and (27). (c) The ratio of J_a to J_b is shown as a function of the detuning Δ . (d) The energy spectrum of the SSH model with $N = 100$, where $r_{2i-2,2i} = 4 \mu\text{m}$ and $r_{2i,2i+1} = 4.1 \mu\text{m}$. The other parameters are taken as $\delta = \Omega_p = 2\pi \times 1 \text{ MHz}$, $\Omega = 0.05\Omega_p$, and $\Delta = 300\Omega_p$.

shown as

$$\tilde{J}_a = J_a e^{ik_r r_{2i-1,2i}}, \quad \tilde{J}_b = J_b e^{ik_r r_{2i,2i+1}}. \quad (34)$$

As shown in Figs. 10(c) and 10(d), under the same parameters, the values of $|J_a/J_b|$ and the energy-band structures of the system do not change, regardless of whether the wave vector \mathbf{k} is considered or not. It is just that the forms of two edge states become $|\Psi\rangle_{\text{edge}} \simeq (e^{ik_z z_1} \sigma_1^+ |gg \dots g\rangle_N \pm e^{ik_z z_N} \sigma_N^+ |gg \dots g\rangle_N) / \sqrt{2}$ for large N .

For the chiral motion of atomic excitation, in order to avoid introducing more relative phases, the propagation directions of the laser fields are redetermined. By adjusting the direction of the external magnetic field, the quantization z axis is redefined as the direction perpendicular to the regular triangle plane. With $r = 4.1 \mu\text{m}$, the radius of a circle surrounded by three atoms is about $2.4 \mu\text{m}$. The collective or independent addressing of atoms can be realized by adjusting the size of the laser beam waist. Accordingly, the global laser fields Ω_{pi} propagate along the z axis and the local laser fields Ω_{i1} and Ω_{i2} propagate perpendicular to the z axis. After defining the center-position coordinates of the regular triangular plane as $(0, 0, 0)$, the phase factors are brought by the weak laser fields, while that brought by the strong fields can be ignored. As shown in Figs. 11(a) and 11(b), we have discussed two situations, one of which is that the effective wave vectors \mathbf{k}_i of weak fields Ω_i are orthogonal to the atomic position \mathbf{r}_i , while the other one is that the weak fields Ω_i propagate in the same direction, such as along a straight line perpendicular to atoms 1 and 2. The piecewise constant Hamiltonian (23)

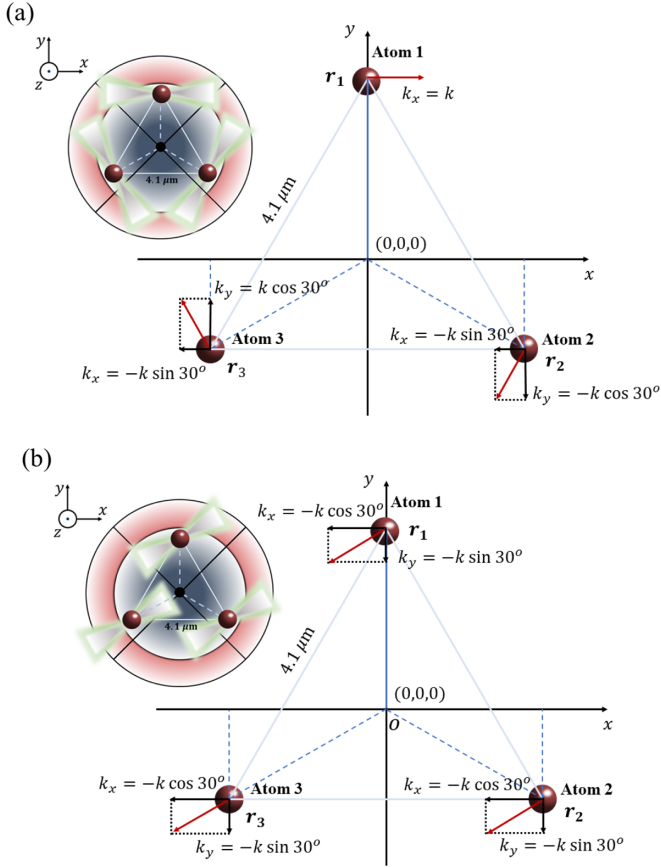


FIG. 11. The feasible experimental structure for the equilateral triangle structure, where the global laser fields Ω_{p1} and Ω_{p2} are counterpropagating along the z axis. (a) The effective wave vectors \mathbf{k}_i of weak fields Ω_i are orthogonal to the atomic position \mathbf{r}_i . (b) The weak fields Ω_i propagate along a straight line perpendicular to atoms 1 and 2.

can be rewritten as

$$H_i = \Omega_i e^{-i\mathbf{k}_i \cdot \mathbf{r}_i} |r_i\rangle \langle g_i| + \sum_{j=1}^4 \Omega_p |r_j\rangle \langle e_j| + \text{H.c.} \\ + \delta |g_j\rangle \langle g_j| + \Delta |e_j\rangle \langle e_j| + \sum_{j < k} \mathcal{U}_{jk} |r_j r_k\rangle \langle r_j r_k|, \quad (35)$$

with effective wave vector $k_i \simeq 5.35 \times 10^6 \text{ m}^{-1}$ introduced by Ω_i . Taking $\bar{\tau}_{ac} = 0.12425 \text{ } \mu\text{s}$ as an example, Figs. 12(a) and 12(b) show the excited population transport between atoms corresponding to the experimental structure shown in Fig. 11(a) and 11(b), respectively. It proves that the relative phases do not affect the chiral motion of atomic excitation.

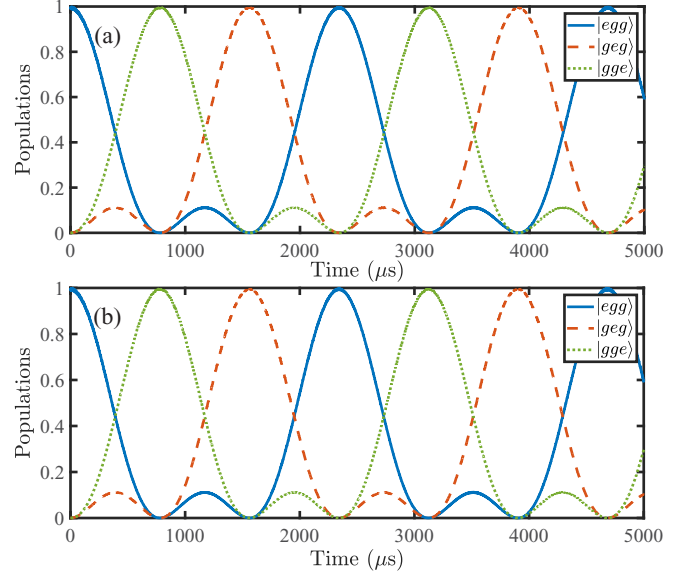


FIG. 12. The dynamics of the chiral motion of atomic excitation with $\bar{\tau}_{ac} = 0.12425 \text{ } \mu\text{s}$. Panel (a) corresponds to the experimental structure shown in Fig. 11(a). Panel (b) corresponds to the experimental structure shown in Fig. 11(b). The other parameters are taken as $\delta = \Omega_p = 2\pi \times 1 \text{ MHz}$, $\Omega = 0.05\Omega_p$, $\Delta = 300\Omega_p$, and $r = 4.1 \text{ } \mu\text{m}$.

As shown in Table II, we further study the effective coupling strengths $J_{\text{eff}}^{12(23,31)}$ and the effective phases $\Phi_{12(23,31)}$ in the two cases above. When the wave vectors \mathbf{k}_i of Ω_i are orthogonal to the atomic position \mathbf{r}_i , we have $\mathbf{k}_i \cdot \mathbf{r}_i = 0$. It equals the method without considering \mathbf{k} . In contrast, for the case that the weak fields Ω_i propagate in the same direction, such as along a straight line perpendicular to atoms 1 and 2, the effective phases will change. However, the total phase Φ_z of the system is basically unchanged, which ensures the chiral motion of atomic excitation.

B. Atomic position fluctuation

In Sec. II, we only discuss the impact of systematic error with a fixed atomic position. In fact, the atoms have a spatial extent, which gives rise to fluctuation in position and results in a random fluctuation on the vdW interaction. We repeat numerical simulation of this stochastic process 50 times and average the results, which are shown in Fig. 13.

Considering the random fluctuations, the vdW interaction between nearest-neighbor atoms can be rewritten as $\mathcal{U}'_{j,j+1}(t) = \mathcal{U}_{j,j+1} + F(t)$, where $F(t)$ is assumed as uniformly distributed over the interval $[-a, a]$, which is decided by the fluctuation δr of relative distance caused by random motion of atoms, shown as $F(t)/2\pi = -a + 2a\xi(t) \text{ MHz}$,

TABLE II. The effective coupling strengths and the effective phases correspond to different lighting modes with $\bar{\tau}_{ac} = 0.12425 \text{ } \mu\text{s}$.

Lighting mode	J_{eff}^{12} (kHz)	J_{eff}^{23} (kHz)	J_{eff}^{31} (kHz)	Φ_{12} (π)	Φ_{23} (π)	Φ_{31} (π)	Φ_z (π)
Without considering \mathbf{k}	1.5481	1.5481	1.5479	0.1651	0.1626	0.1651	0.4928
Orthogonal to position \mathbf{r}_i	1.5481	1.5481	1.5479	0.1651	0.1626	0.1651	0.4928
Perpendicular to atoms 1 and 2	1.5481	1.5481	1.5479	0.1651	0.1133	0.2144	0.4928

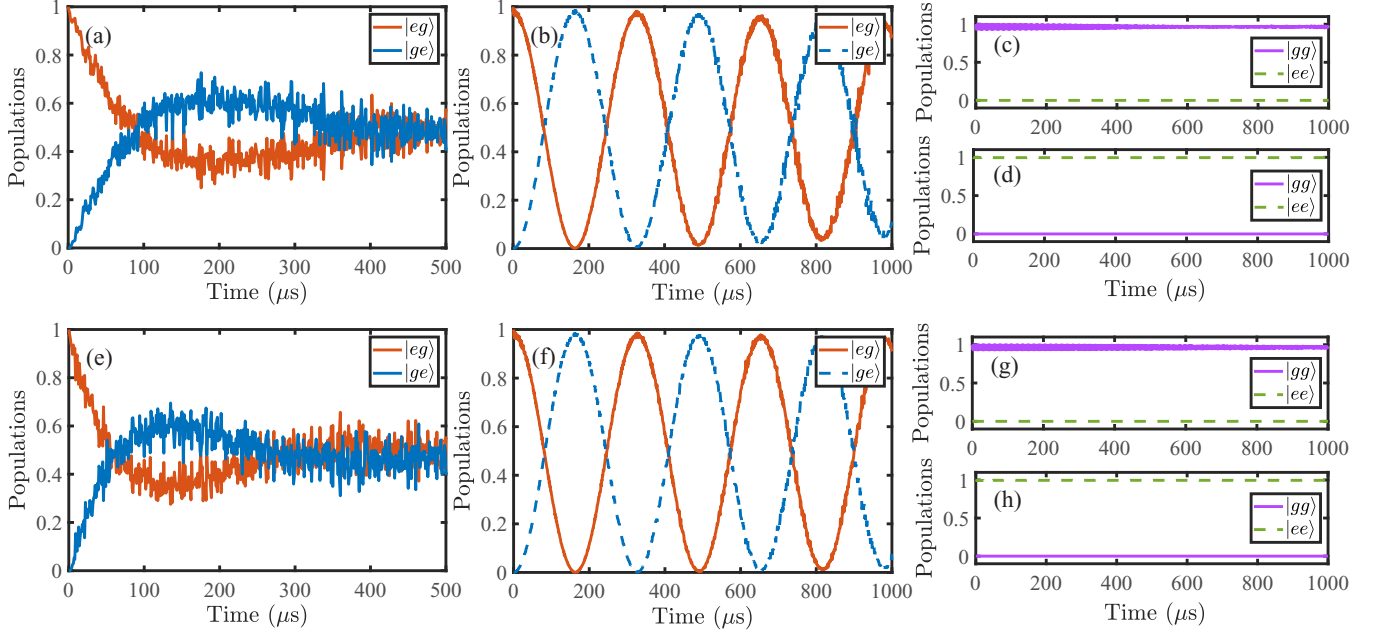


FIG. 13. Transport dynamics considering the position fluctuations. Panels (a) and (e) correspond to populations of states $|eg\rangle$ and $|ge\rangle$ together with considering the random fluctuation obeys the uniform density and standard normal density distribution, respectively. The parameters are $\delta = \Omega_p = 2\pi \times 1$ MHz, $\Omega = 0.05\Omega_p$, $\Delta = 300\Omega_p$, and $\mathcal{U}'_{j,j+1} \simeq 300\Omega_p + F(t)$. (b)–(d) Populations of states $|eg\rangle$, $|ge\rangle$, $|ee\rangle$, and $|gg\rangle$ under the adjusted parameters with $F(t)$ uniformly distributed, respectively. (f)–(h) The dynamics of the system with $F(t)$ obeying the standard normal density distribution. The optimized parameters are $\delta = \Omega_p = 2\pi \times 10$ MHz, $\Omega = 0.1\Omega_p$, $\Delta = 30\Omega_p$, and $\mathcal{U}'_{j,j+1} \simeq 10\Omega_p + F(t)$.

in which $\xi(t)$ is a uniformly distributed random number in the interval $[0,1]$. With $F(t)$ changing every microsecond, the quantum state transport is damaged under the original parameters $\delta = \Omega_p = 2\pi \times 1$ MHz, $\Omega = 0.05\Omega_p$, and $\mathcal{U}_{j,j+1} = \Delta = 300\Omega_p$ with $a = 3$ as shown in Fig. 13(a). The corresponding fluctuation of relative distance is about $\delta r \simeq 0.01 \mu\text{m}$. To solve this problem and weaken the influence induced by fluctuation, we take out the condition $\mathcal{U}_{j,j+1} = \Delta$ and adjust the parameters as $\delta = \Omega_p = 2\pi \times 10$ MHz, $\Omega = 0.1\Omega_p$, $\Delta = 30\Omega_p$, and $\mathcal{U}_{j,j+1} = 10\Omega_p$. The corresponding dynamics of the system after optimization is shown in Fig. 13(b). The distinct Rabi oscillation of populations between states $|eg\rangle$ and $|ge\rangle$ can be observed. In addition, we perform another simulation with $F(t)$ obeying the standard normal distribution shown as $F(t)/2\pi = \sqrt{-2\ln\xi_1(t)}\cos[2\pi\xi_2(t)]$ MHz with $\delta r \simeq 0.01 \mu\text{m}$. The dynamics under original and optimized parameters are shown in Figs. 13(e) and 13(f), respectively. In addition, the evolutions of states $|ee\rangle$ and $|gg\rangle$ under the optimized parameters with $F(t)$ considered as uniform and standard normal distribution are respectively shown in Figs. 13(c) [13(d)] and 13(g) [13(h)], which prove that the dynamics of the system accord with the Heisenberg XX spin chain for two particles.

The reason why the scheme based on the optimized parameters is more robust against position fluctuations can be clearly understood by analyzing the relationship between the effective coupling strength and the change of atomic position. The effective coupling strength holds the same form as Eq. (20) with $\mathcal{U}_{j,j+1}(F) = \mathcal{U}_{j,j+1} + F$ where $F/2\pi \in [-3, 3]$ MHz represents the variation of the vdW interaction caused by the

change of atomic position. Thus we have the derivation of $J_{j,j+1}(F)$ to F

$$\frac{dJ_{j,j+1}(F)}{dF} = \frac{(\delta - \Delta)^2 \Omega^2 \Omega_p^2}{[\delta(\delta^2 - \eta_{j,j+1}) - (\delta^2 - 2\Omega_p^2)\mathcal{U}_{j,j+1}(F)]^2}, \quad (36)$$

where $\eta_{j,j+1} = 4\Omega_p^2 + \Delta^2 - \mathcal{U}_{j,j+1}(F)\Delta$. As shown in Fig. 14, $J_{j,j+1}(F)$ changes more dramatically with F under the original parameters [there is a singularity which can be found directly from Eq. (16) as $\mathcal{U}_{j,j+1} = -\delta$]. In contrast, under the optimized parameters, $dJ_{j,j+1}(F)/dF$ is close to zero, which guarantees that the system dynamics is more robust against the fluctuation of the vdW interaction.

C. Effectiveness of van der Waals interaction

Strictly speaking, the perturbative-calculation-based estimation of the short-range vdW interaction intensity between Rydberg states is not working at all, because splittings between energy levels are smaller than interaction energies. To find a more practical system parameter, we rewrite the Hamiltonian of the system as

$$H_I^{(N)} = \sum_{j=1}^N \Omega_j |r_j\rangle \langle g_j| + \Omega_p |r_j\rangle \langle e_j| + \text{H.c.} + \delta |g_j\rangle \langle g_j| + \Delta |e_j\rangle \langle e_j| + H_{\text{int}}^{rr}, \quad (37)$$

where H_{int}^{rr} presents the interactions between Rydberg state $|r\rangle = |73S_{1/2}\rangle$ and the states with similar energy and quantum numbers. After diagonalizing the Hamiltonian of these

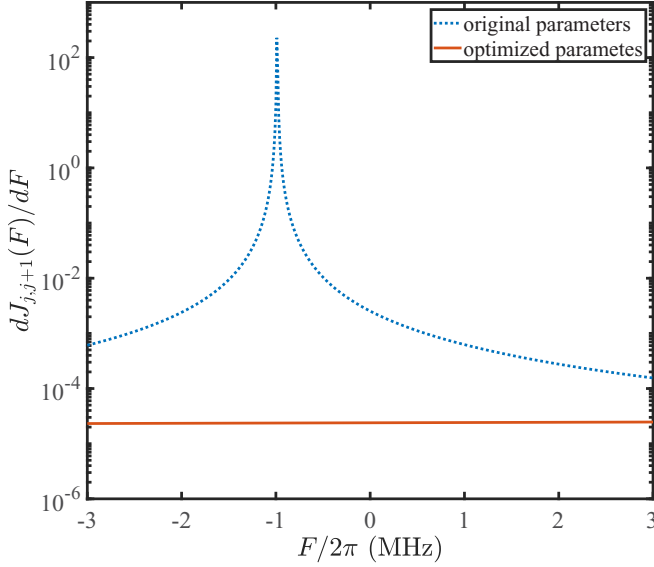


FIG. 14. The derivation of $J_{j,j+1}(F)$ to F under the original and optimized parameters. The original parameters are taken as $\delta = \Omega_p = 2\pi \times 1$ MHz, $\Omega = 0.05\Omega_p$, $\Delta = 300\Omega_p$, and $\mathcal{U}_{j,j+1} = 300\Omega_p$. The optimized parameters are taken as $\delta = \Omega_p = 2\pi \times 10$ MHz, $\Omega = 0.1\Omega_p$, $\Delta = 30\Omega_p$, and $\mathcal{U}_{j,j+1} = 10\Omega_p$.

quantum states (principal quantum number $|n - 73| \leq 5$ and azimuthal quantum number $|L| \leq 5$) based on the open software “ALKALI RYDBERG CALCULATOR” [65], the energy map is shown in Fig. 15 and the population of the state $|rr\rangle = |73S_{1/2}, m_j = 1/2; 73S_{1/2}, m_j = 1/2\rangle$ in the diagonalized state increases as the red color deepens. We focus on the three eigenstates denoted as $|\phi_1\rangle$, $|\phi_2\rangle$, and $|\phi_3\rangle$ in Fig. 15 with highest population of $|rr\rangle$, where $|\phi_1\rangle$ is mainly constructed by $\{|rr\rangle, |72P_{3/2}, m_j = 1/2; 73P_{3/2}, m_j = 1/2\rangle, |73P_{3/2}, m_j = 1/2; 72P_{3/2}, m_j = 1/2\rangle\}$, $|\phi_2\rangle$ is mainly constructed by $\{|rr\rangle, |73P_{3/2}, m_j =$

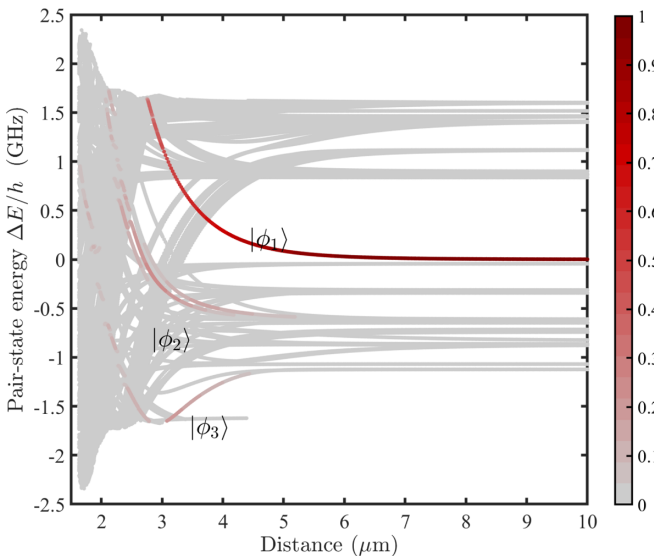


FIG. 15. The pair potentials of ^{87}Rb atoms around the defined pair state $|rr\rangle = |73S_{1/2}, m_j = 1/2; 73S_{1/2}, m_j = 1/2\rangle$. The red color denotes the overlap of the eigenstates with $|rr\rangle$.

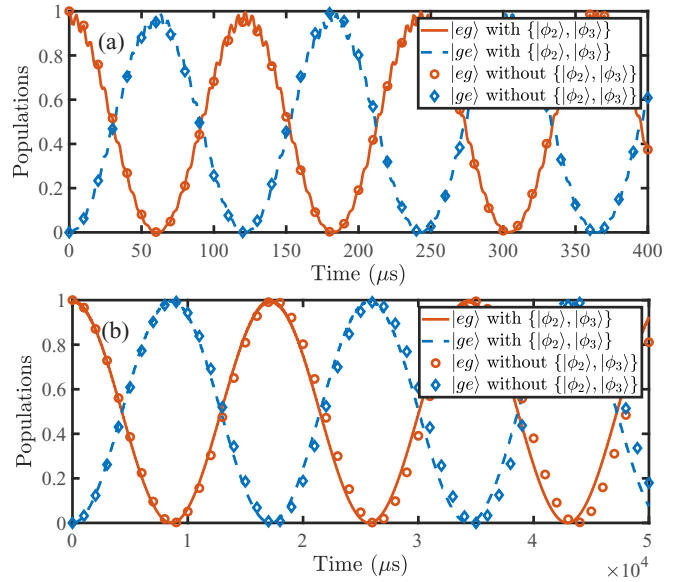


FIG. 16. Transport dynamics of states $|eg\rangle$ (red) and $|ge\rangle$ (blue) with and without states $|\phi_2\rangle, |\phi_3\rangle$. Panel (a) corresponds to the system with $\Delta U = 0$. Panel (b) corresponds to the system with $\Delta U = -2\pi \times 50$ MHz. The other parameters are taken as $\Omega_j = 0.05\Omega_p$, $E_1 = 2\pi \times 300$ MHz, $E_2 = -2\pi \times 511.25$ MHz, $E_3 = -2\pi \times 1258.83$ MHz, $\alpha_1 = \sqrt{0.72}$, $\alpha_2 = \sqrt{0.126}$, and $\alpha_3 = \sqrt{0.088}$.

$1/2; 72P_{3/2}, m_j = 1/2\rangle, |72P_{3/2}, m_j = 1/2; 73P_{3/2}, m_j = 1/2\rangle, |74S_{1/2}, m_j = 1/2; 72S_{1/2}, m_j = 1/2\rangle, |72S_{1/2}, m_j = 1/2; 74S_{1/2}, m_j = 1/2\rangle\}$, while $|\phi_3\rangle$ is mainly constructed by $\{|rr\rangle, |74S_{1/2}, m_j = 1/2; 72S_{1/2}, m_j = 1/2\rangle, |72S_{1/2}, m_j = 1/2; 74S_{1/2}, m_j = 1/2\rangle, |73P_{1/2}, m_j = 1/2; 72P_{1/2}, m_j = 1/2\rangle\}$. Then we have $H_{int}^{rr} \approx E_1|\phi_1\rangle\langle\phi_1| + E_2|\phi_2\rangle\langle\phi_2| + E_3|\phi_3\rangle\langle\phi_3|$ and $|rr\rangle \approx \alpha_1|\phi_1\rangle + \alpha_2|\phi_2\rangle + \alpha_3|\phi_3\rangle$, where α_1, α_2 , and α_3 are the probability amplitudes of state $|rr\rangle$. Taking into account the large detuning and weak-coupling strength $\alpha_{2(3)}\Omega_p$ between $\{|er\rangle, |re\rangle\}$ and $\{|\phi_2\rangle, |\phi_3\rangle\}$, only $|\phi_1\rangle$ contributes and $\{|\phi_2\rangle, |\phi_3\rangle\}$ can be neglected as high-frequency terms.

The dynamics of systems with and without considering $\{|\phi_2\rangle, |\phi_3\rangle\}$ are shown in Fig. 16 for $r_{j,j+1} = 3.99 \mu\text{m}$. Figure 16(a) corresponds to the system satisfying the resonance condition $E_1 = \Delta$, while Fig. 16(b) includes the deviation of unconventional Rydberg pumping conditions with $E_1 \neq \Delta$ and $\Delta U = E_1 - \Delta = -2\pi \times 50$ MHz. The other parameters are taken as $\delta = \Omega_p = 2\pi \times 1$ MHz, $\Omega_j = 0.05\Omega_p$ MHz, $E_1 = 2\pi \times 300$ MHz, $E_2 = -2\pi \times 511.25$ MHz, $E_3 = -2\pi \times 1258.83$ MHz, $\alpha_1 = \sqrt{0.72}$, $\alpha_2 = \sqrt{0.126}$, and $\alpha_3 = \sqrt{0.088}$. The corresponding numerical results prove that, within a certain range of detuning ΔU , $\{|\phi_2\rangle, |\phi_3\rangle\}$ can always be safely neglected. Incorporating the effective operator method with the above analysis, we obtain the effective coupling strength with and without ΔU as

$$J_{j,j+1} = \frac{\Omega_j \Omega_{j+1} \alpha_1^2 \Omega_p^2}{\delta^3 - 2\delta \alpha_1^2 \Omega_p^2}, \quad (38)$$

and

$$J_{j,j+1} = \frac{\Omega_j \Omega_{j+1} \Omega_p^2 \zeta}{\delta^2(\delta - \Delta U)(\delta - \Delta) - 2\zeta \delta \Omega_p^2}, \quad (39)$$

where $\zeta = \delta + \alpha_1^2 \delta - \alpha_1^2 \Delta - \Delta U$. The correction shown in Eqs. (38) and (39) will not affect the conclusions we obtained before. For perfect quantum state transfer protocol and the chiral motion of atomic excitation, by comparing the forms of $J_{j,j+1}$ in Eqs. (38) and (15), it can be found that the system dynamics remains unchanged by setting $\Omega_p = 2\pi(1/\alpha_1)$ MHz. For the topological model, the corresponding topological phase can always be achieved by modulating the parameter Δ and the atomic separations.

VI. CONCLUSION

In conclusion, we have proposed a theoretical framework for studying quantum state transfer schemes inside the ground-state manifold of neutral atoms by only combining the diagonal vdW interaction with the unconventional Rydberg pumping condition. The scheme successfully realizes the Heisenberg XX spin-chain dynamics restricted in the single-excitation manifold. Meanwhile, depending on the choice of parameters, the system dynamics can be equivalent to a second-order process only related to weak fields and the perfect quantum state transfer is realized by simply regulating the weak fields of atoms. A 1D SSH model is then constructed by changing the distance between atoms, and the system can be flexibly changed from the topological trivial phase to a non-trivial phase by adjusting the detuning Δ . Finally, a method to realize the chiral motion of atomic excitation is provided in the equilateral triangle structure. A total flux $\Phi_z = \pm\pi/2$ can be obtained by periodically modulating the weak pulses without introducing any other external fields. In a word, we can get abundant physical pictures by using such a simple physical system, and we hope that our work may pave a new avenue for quantum simulation of neutral atomic system.

ACKNOWLEDGMENTS

The author would like to thank Dr. Kuan Zhang and Professor Lin Li for helpful comments and suggestions. The anonymous reviewers are also thanked for constructive comments that helped in improving the quality of this paper. This work is supported by National Natural Science Foundation of China (NSFC) under Grants No. 11774047 and No. 12174048. J.B.Y. acknowledges the supports from the National Research Foundation Singapore (QEP-SF1) and A*STAR Career Development Award (SC23/21-8007EP). W.L. acknowledges support from the EPSRC through Grant No. EP/R04340X/1 via the QuantERA project ‘‘ERYQSenS,’’ the Royal Society Grant No. IEC\NSFC\181078.

APPENDIX A: THE $\sqrt{\text{SWAP}}$ GATE

For a diatomic model, our method can also be used to realize the $\sqrt{\text{SWAP}}$ gate shown as

$$\sqrt{\text{SWAP}} = \begin{bmatrix} 1 & 0 & 0 & 0 \\ 0 & \frac{1}{2}(1+i) & \frac{1}{2}(1-i) & 0 \\ 0 & \frac{1}{2}(1-i) & \frac{1}{2}(1+i) & 0 \\ 0 & 0 & 0 & 1 \end{bmatrix}. \quad (\text{A1})$$

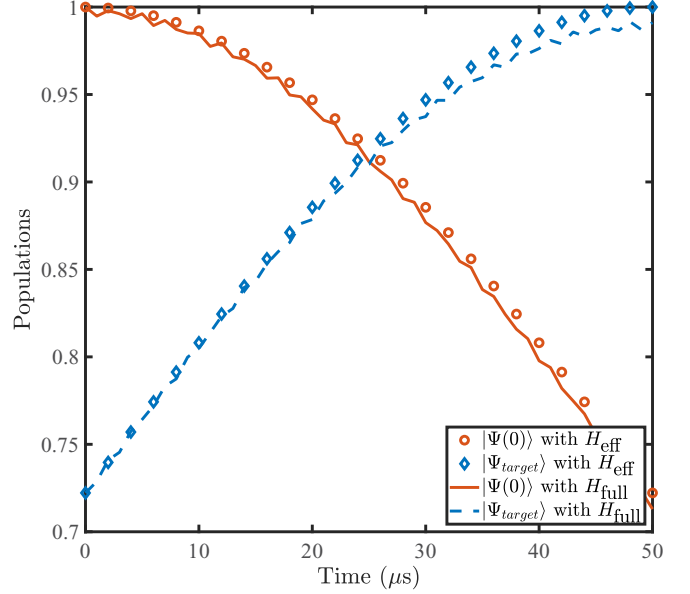


FIG. 17. Transport dynamics of diatomic model governed by the full Hamiltonian (A2) after shifting the energy of $|e_i\rangle$ and $|g_i\rangle$ and the effective Hamiltonian of Eq. (A4), respectively. The initial state is $|\Psi(0)\rangle = 1/\sqrt{3}(|eg\rangle + |gg\rangle + |ee\rangle)$ and the parameters are taken as $\delta = \Omega_p = 2\pi \times 1$ MHz, $\Omega = 0.05\Omega_p$, and $\Delta = 300\Omega_p$.

In the interaction picture, the Hamiltonian of the system reads

$$H_I^{(2)} = \sum_{j=1}^2 \Omega_j e^{i\delta t} |r_j\rangle \langle g_j| + \Omega_p e^{i\Delta t} |r_j\rangle \langle e_j| + \text{H.c.} + \mathcal{U}|rr\rangle \langle rr|, \quad (\text{A2})$$

and the effective Hamiltonian is

$$H_{\text{eff}} = J_{\text{eff}}|ge\rangle \langle eg| + \text{H.c.} + S_1(|ge\rangle \langle ge| + |eg\rangle \langle eg|) + S_2|gg\rangle \langle gg| + S_3|ee\rangle \langle ee|, \quad (\text{A3})$$

where $J_{\text{eff}} = \Omega_1 \Omega_2 \Omega_p^2 / (\delta^3 - 2\delta \Omega_p^2)$, $S_1 = \Omega_1 \Omega_2 (\delta^2 - \Omega_p^2) / (\delta^3 - 2\delta \Omega_p^2) + \Omega_p^2 / \Delta$, $S_2 = (\Omega_1^2 + \Omega_2^2) / \delta$, $S_3 = 2\Omega_p^2 / \Delta$. The energy of states $|ee\rangle$ and $|gg\rangle$ can be shifted to zero by Stark shifts through coupling to extra states off-resonantly. Under the condition $\delta = \Omega_p$ and $\Omega_1 = -\Omega_2 = \Omega$, the effective Hamiltonian can be simplified as

$$H_{\text{eff}} = \frac{\Omega^2}{\delta} (|eg\rangle \langle ge| + |ge\rangle \langle eg|) - \frac{\Omega^2}{\delta} (|eg\rangle \langle eg| + |ge\rangle \langle ge|). \quad (\text{A4})$$

The system governed by this Hamiltonian can realize a quantum $\sqrt{\text{SWAP}}$ gate with $t = \delta\pi/4\Omega^2$. Corresponding population evolutions under the Hamiltonians (A2) and (A4) are respectively shown in Fig. 17, where the parameters are $\delta = \Omega_p = 2\pi \times 1$ MHz, $\Omega = 0.05\Omega_p$, and $\Delta = 300\Omega_p$. At $t = 50 \mu\text{s}$, the population of state $1/\sqrt{3}(|eg\rangle + |gg\rangle + |ee\rangle)$ is transferred to $|\Psi_{\text{target}}\rangle = 1/\sqrt{3}[1/2(1+i)|eg\rangle + 1/2(1-i)|ge\rangle + |gg\rangle + |ee\rangle]$.

APPENDIX B: BUILDING BLOCK FOR CHIRAL MOTION OF ATOMIC EXCITATION

To construct the chiral motion of atomic excitation, we introduce the piecewise Hamiltonian:

$$H(t) = \begin{cases} H_1, & t \in [0, T/3) \\ H_2, & t \in [T/3, 2T/3) \\ H_3, & t \in [2T/3, T) \end{cases} \quad (\text{B1})$$

where

$$H_i = \Omega_i e^{-i\delta t} |r_i\rangle \langle g_i| + \sum_{j=1}^3 \Omega_p e^{-i\Delta t} |r_j\rangle \langle e_j| + \text{H.c.} \\ + \sum_{j<k} \mathcal{U}_{jk} |r_j r_k\rangle \langle r_j r_k|. \quad (\text{B2})$$

Since H_i ($i = 1, 2, 3$) do not commute with each other, this periodical driving will induce the effective coupling strengths

associating with the period T and the phases between ground states. Because the computational space is very large, we calculate the effective Hamiltonian by bonding analytic and numerical methods together. For a given τ , the system Hamiltonian can be numerically obtained as a large matrix and the effective Hamiltonian can be expressed in logarithmic form as

$$H_{\text{eff}} = \frac{i}{T} \ln(e^{-iH_3\tau} e^{-iH_2\tau} e^{-iH_1\tau}). \quad (\text{B3})$$

According to Eq. (B1), under the unconventional Rydberg pumping condition and in the limit $\Delta \gg \Omega_p$, the highly oscillating term proportional to Δ can be neglected. Thus, the dynamics is restricted in states $|egg\rangle, |egr\rangle, |rgr\rangle, |rge\rangle, |gge\rangle, |gre\rangle, |grr\rangle, |ger\rangle, |geg\rangle, |reg\rangle, |rrg\rangle$, and $|erg\rangle$. To simplify computational space, we only consider the subspace constructed by these 12 states in the subsequent calculations. To obtain the specific value of phases, we first numerically expand the effective Hamiltonian as a 12×12 matrix with some definite value of τ read as

$$H = \begin{bmatrix} \rho_{1,1} & \rho_{1,2} & \rho_{1,3} & \rho_{1,4} & \rho_{1,5} & \rho_{1,6} & \rho_{1,7} & \rho_{1,8} & \rho_{1,9} & \rho_{1,10} & \rho_{1,11} & \rho_{1,12} \\ \rho_{1,2}^* & \rho_{2,2} & \rho_{2,3} & \rho_{2,4} & \rho_{2,5} & \rho_{2,6} & \rho_{2,7} & \rho_{2,8} & \rho_{2,9} & \rho_{2,10} & \rho_{2,11} & \rho_{2,12} \\ \rho_{1,3}^* & \rho_{2,3}^* & \rho_{3,3} & \rho_{3,4} & \rho_{3,5} & \rho_{3,6} & \rho_{3,7} & \rho_{3,8} & \rho_{3,9} & \rho_{3,10} & \rho_{3,11} & \rho_{3,12} \\ \rho_{1,4}^* & \rho_{2,4}^* & \rho_{3,4}^* & \rho_{4,4} & \rho_{4,5} & \rho_{4,6} & \rho_{4,7} & \rho_{4,8} & \rho_{4,9} & \rho_{4,10} & \rho_{4,11} & \rho_{4,12} \\ \rho_{1,5}^* & \rho_{2,5}^* & \rho_{3,5}^* & \rho_{4,5}^* & \rho_{5,5} & \rho_{5,6} & \rho_{5,7} & \rho_{5,8} & \rho_{5,9} & \rho_{5,10} & \rho_{5,11} & \rho_{5,12} \\ \rho_{1,6}^* & \rho_{2,6}^* & \rho_{3,6}^* & \rho_{4,6}^* & \rho_{5,6}^* & \rho_{6,6} & \rho_{6,7} & \rho_{6,8} & \rho_{6,9} & \rho_{6,10} & \rho_{6,11} & \rho_{6,12} \\ \rho_{1,7}^* & \rho_{2,7}^* & \rho_{3,7}^* & \rho_{4,7}^* & \rho_{5,7}^* & \rho_{6,7}^* & \rho_{7,7} & \rho_{7,8} & \rho_{7,9} & \rho_{7,10} & \rho_{7,11} & \rho_{7,12} \\ \rho_{1,8}^* & \rho_{2,8}^* & \rho_{3,8}^* & \rho_{4,8}^* & \rho_{5,8}^* & \rho_{6,8}^* & \rho_{7,8}^* & \rho_{8,8} & \rho_{8,9} & \rho_{8,10} & \rho_{8,11} & \rho_{8,12} \\ \rho_{1,9}^* & \rho_{2,9}^* & \rho_{3,9}^* & \rho_{4,9}^* & \rho_{5,9}^* & \rho_{6,9}^* & \rho_{7,9}^* & \rho_{8,9}^* & \rho_{9,9} & \rho_{9,10} & \rho_{9,11} & \rho_{9,12} \\ \rho_{1,10}^* & \rho_{2,10}^* & \rho_{3,10}^* & \rho_{4,10}^* & \rho_{5,10}^* & \rho_{6,10}^* & \rho_{7,10}^* & \rho_{8,10}^* & \rho_{9,10}^* & \rho_{10,10} & \rho_{10,11} & \rho_{10,12} \\ \rho_{1,11}^* & \rho_{2,11}^* & \rho_{3,11}^* & \rho_{4,11}^* & \rho_{5,11}^* & \rho_{6,11}^* & \rho_{7,11}^* & \rho_{8,11}^* & \rho_{9,11}^* & \rho_{10,11}^* & \rho_{11,11} & \rho_{11,12} \\ \rho_{1,12}^* & \rho_{2,12}^* & \rho_{3,12}^* & \rho_{4,12}^* & \rho_{5,12}^* & \rho_{6,12}^* & \rho_{7,12}^* & \rho_{8,12}^* & \rho_{9,12}^* & \rho_{10,12}^* & \rho_{11,12}^* & \rho_{12,12} \end{bmatrix}. \quad (\text{B4})$$

The order of basis vectors is taken as $|egg\rangle, |erg\rangle, |rrg\rangle, |reg\rangle, |geg\rangle, |ger\rangle, |grr\rangle, |gre\rangle, |gge\rangle, |rge\rangle, |rgr\rangle$, and $|egr\rangle$. Then the Hamiltonian corresponding to the coupling between arbitrary ground states respectively read

$$H_{11} = \begin{bmatrix} \rho_{1,1} & \rho_{1,2} & \rho_{1,3} & \rho_{1,4} & \rho_{1,5} \\ \rho_{1,2}^* & \rho_{2,2} & \rho_{2,3} & \rho_{2,4} & \rho_{2,5} \\ \rho_{1,3}^* & \rho_{2,3}^* & \rho_{3,3} & \rho_{3,4} & \rho_{3,5} \\ \rho_{1,4}^* & \rho_{2,4}^* & \rho_{3,4}^* & \rho_{4,4} & \rho_{4,5} \\ \rho_{1,5}^* & \rho_{2,5}^* & \rho_{3,5}^* & \rho_{4,5}^* & \rho_{5,5} \end{bmatrix}, \quad (\text{B5})$$

$$H_{12} = \begin{bmatrix} \rho_{5,5} & \rho_{5,6} & \rho_{5,7} & \rho_{5,8} & \rho_{5,9} \\ \rho_{5,6}^* & \rho_{6,6} & \rho_{6,7} & \rho_{6,8} & \rho_{6,9} \\ \rho_{5,7}^* & \rho_{6,7}^* & \rho_{7,7} & \rho_{7,8} & \rho_{7,9} \\ \rho_{5,8}^* & \rho_{6,8}^* & \rho_{7,8}^* & \rho_{8,8} & \rho_{8,9} \\ \rho_{5,9}^* & \rho_{6,9}^* & \rho_{7,9}^* & \rho_{8,9}^* & \rho_{9,9} \end{bmatrix}, \quad (\text{B6})$$

$$H_{13} = \begin{bmatrix} \rho_{9,9} & \rho_{9,10} & \rho_{9,11} & \rho_{9,12} & \rho_{1,9}^* \\ \rho_{9,10}^* & \rho_{10,10} & \rho_{10,11} & \rho_{10,12} & \rho_{1,10}^* \\ \rho_{9,11}^* & \rho_{10,11}^* & \rho_{11,11} & \rho_{11,12} & \rho_{1,11}^* \\ \rho_{9,12}^* & \rho_{10,12}^* & \rho_{11,12}^* & \rho_{12,12} & \rho_{1,12}^* \\ \rho_{1,9} & \rho_{1,10} & \rho_{1,11} & \rho_{1,12} & \rho_{1,1} \end{bmatrix}. \quad (\text{B7})$$

Combined with above three 5×5 matrices, the effective couplings between any two ground states of $\{|egg\rangle, |geg\rangle, |gge\rangle\}$

can be obtained via second-order perturbation theory. Taking H_{11} as an example, the specified calculation process is illustrated below. First we diagonalized the strong-coupling part which correspond to the 3×3 matrix in the middle of H_{11} . Then the Hamiltonian of this part can be represented by its eigenvalues and eigenvectors as

$$H_{\text{sc}} = E_1 |\psi_1\rangle \langle \psi_1| + E_2 |\psi_2\rangle \langle \psi_2| + E_3 |\psi_3\rangle \langle \psi_3|, \quad (\text{B8})$$

where the eigenvectors are given by

$$|\psi_1\rangle = C_{11}|erg\rangle + C_{12}|rrg\rangle + C_{13}|reg\rangle,$$

$$|\psi_2\rangle = C_{21}|erg\rangle + C_{22}|rrg\rangle + C_{23}|reg\rangle,$$

$$|\psi_3\rangle = C_{31}|erg\rangle + C_{32}|rrg\rangle + C_{33}|reg\rangle.$$

Through the transformation of representation, the basis vectors can be changed to states $|egg\rangle, |geg\rangle$, and $|\psi_i\rangle$ ($i = 1, 2, 3$),

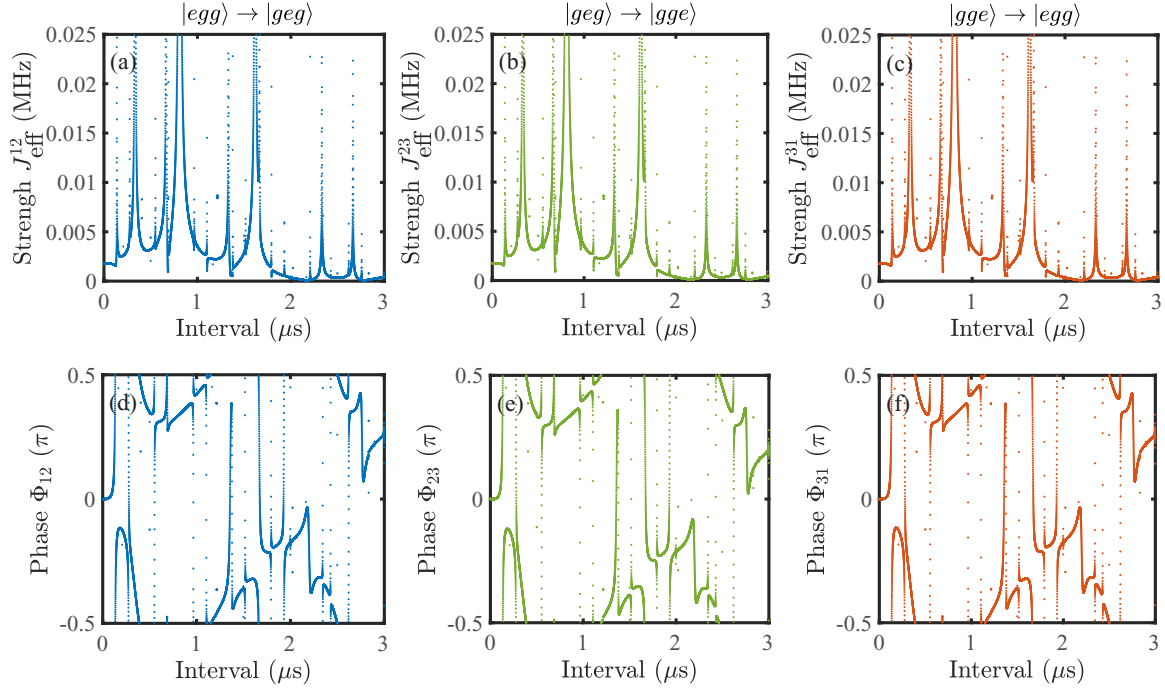


FIG. 18. The effective coupling strengths and phases between arbitrary ground states induced by periodical driving. The parameters are taken as $\delta = \Omega_p = 2\pi \times 1$ MHz, $\Omega_i = 0.05\Omega_p$, and $\Delta = 2\pi \times 300$ MHz.

and Eq. (B5) changes to

$$H_{11} = \begin{bmatrix} \rho_{1,1} & \tilde{\rho}_{1,2} & \tilde{\rho}_{1,3} & \tilde{\rho}_{1,4} & \rho_{1,5} \\ \tilde{\rho}_{1,2}^* & E_1 & 0 & 0 & \tilde{\rho}_{2,5} \\ \tilde{\rho}_{1,3}^* & 0 & E_2 & 0 & \tilde{\rho}_{3,5} \\ \tilde{\rho}_{1,4}^* & 0 & 0 & E_3 & \tilde{\rho}_{4,5} \\ \rho_{1,5}^* & \tilde{\rho}_{2,5}^* & \tilde{\rho}_{3,5}^* & \tilde{\rho}_{4,5}^* & \rho_{5,5} \end{bmatrix}, \quad (\text{B9})$$

where

$$\tilde{\rho}_{1,2} = \rho_{1,2}C_{11} + \rho_{1,3}C_{12} + \rho_{1,4}C_{13},$$

$$\tilde{\rho}_{1,3} = \rho_{1,2}C_{21} + \rho_{1,3}C_{22} + \rho_{1,4}C_{23},$$

$$\tilde{\rho}_{1,4} = \rho_{1,2}C_{31} + \rho_{1,3}C_{32} + \rho_{1,4}C_{33},$$

$$\tilde{\rho}_{2,5} = \rho_{2,5}C_{11}^* + \rho_{3,5}C_{12}^* + \rho_{4,5}C_{13}^*,$$

$$\tilde{\rho}_{3,5} = \rho_{2,5}C_{21}^* + \rho_{3,5}C_{22}^* + \rho_{4,5}C_{23}^*,$$

$$\tilde{\rho}_{4,5} = \rho_{2,5}C_{31}^* + \rho_{3,5}C_{32}^* + \rho_{4,5}C_{33}^*.$$

According to Eq. (B9), the Raman transition between ground states $|egg\rangle$ and $|geg\rangle$ is assisted by multiple channels, the Hamiltonian of each channel can be written as

$$H_{11}^{(1)} = \tilde{\rho}_{1,2}e^{-iE_1t}|egg\rangle\langle\psi_1| + \tilde{\rho}_{2,5}e^{iE_1t}|\psi_1\rangle\langle geg| + \text{H.c.}, \quad (\text{B10})$$

$$H_{11}^{(2)} = \tilde{\rho}_{1,3}e^{-iE_2t}|egg\rangle\langle\psi_2| + \tilde{\rho}_{3,5}e^{iE_2t}|\psi_2\rangle\langle geg| + \text{H.c.}, \quad (\text{B11})$$

$$H_{11}^{(3)} = \tilde{\rho}_{1,4}e^{-iE_3t}|egg\rangle\langle\psi_3| + \tilde{\rho}_{4,5}e^{iE_3t}|\psi_3\rangle\langle geg| + \text{H.c.} \quad (\text{B12})$$

In the limit of large detunings with $E_1 \gg \tilde{\rho}_{1,2(2,5)}$, $E_2 \gg \tilde{\rho}_{1,3(3,5)}$, and $E_3 \gg \tilde{\rho}_{1,4(4,5)}$, the excited states $|\psi_i\rangle$ can be adiabatically eliminated, and the effective coupling constant of the ground-state transition $|geg\rangle \rightarrow |egg\rangle$ is

$$J_{12} = -J_{\text{eff}}^{12}e^{i\Phi_{12}} = \rho_{1,5} - \frac{\tilde{\rho}_{1,2}\tilde{\rho}_{2,5}}{E_1} - \frac{\tilde{\rho}_{1,3}\tilde{\rho}_{3,5}}{E_2} - \frac{\tilde{\rho}_{1,4}\tilde{\rho}_{4,5}}{E_3}. \quad (\text{B13})$$

Thus, the coupling strength and the induced phase read

$$J_{\text{eff}}^{12} = |J_{12}|, \quad \Phi_{12} = \frac{1}{\pi} \arctan \left[\frac{\text{Im}(J_{12})}{\text{Re}(J_{12})} \right]. \quad (\text{B14})$$

The same operations can be performed for the other two processes $|egg\rangle \rightarrow |gge\rangle$ and $|gge\rangle \rightarrow |geg\rangle$ and the effective Hamiltonian of the whole system can be obtained as

$$H_{\text{eff}} = -J_{\text{eff}}^{12}e^{i\Phi_{12}}|egg\rangle\langle geg| - J_{\text{eff}}^{23}e^{i\Phi_{23}}|geg\rangle\langle gge| - J_{\text{eff}}^{31}e^{i\Phi_{31}}|gge\rangle\langle egg| + \text{H.c.}, \quad (\text{B15})$$

which can successfully lead to a chiral motion of atomic excitation with $\Phi_{12} + \Phi_{23} + \Phi_{31} = \pm\pi/2$. Figure 18 shows the numerical results of the effective couplings J_{eff}^{ij} and induced phases Φ_{ij} ($i, j = 12, 23, 31$) between arbitrary ground states with different time intervals τ , in which we calculate the original Hamiltonian shown as a 27×27 matrix for higher precision. To promise results consistent with the ground-state dynamics, we keep the convergent results and discard the divergent results. Figures 19(a)–19(c) characterize the change of $\tilde{\tau}$ with Ω , δ , and Ω_p , respectively. It illustrates that $\tilde{\tau}$ is mainly related to δ and Ω_p . Meanwhile, on average, the homologous effective coupling strengths J_{eff} are shown in Figs. 19(d)–19(f). The corresponding $\tilde{\tau}$ here has ideal values which may be difficult to accurately control in experiments. To test the maneuverability, we reduce the accuracy of the

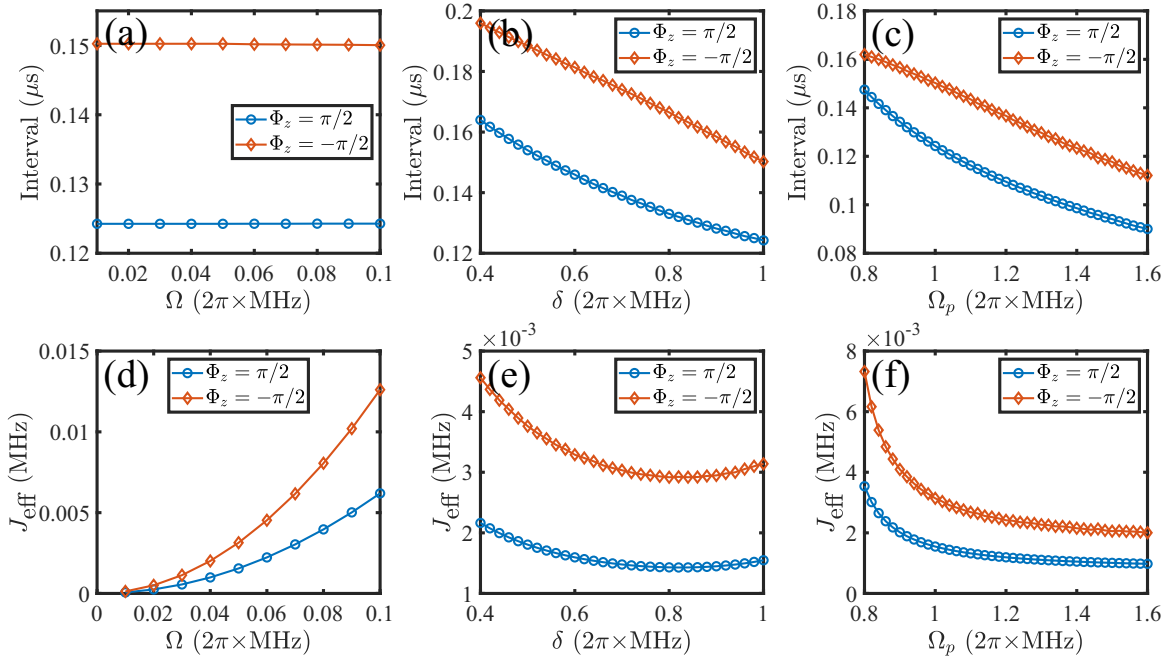


FIG. 19. Panels (a) and (d) respectively show the change of $\bar{\tau}$ and J_{eff} with Ω . The other parameters are $\delta = \Omega_p = 2\pi \times 1$ MHz, $\Delta = 300\Omega_p$. Panels (b) and (e) respectively show the change of $\bar{\tau}$ and J_{eff} with δ . The other parameters are $\Omega_p = 2\pi \times 1$ MHz, $\Omega = 2\pi \times 0.05$ MHz, $\Delta = 300\Omega_p$. Panels (c) and (f) respectively show the change of $\bar{\tau}$ and J_{eff} with Ω_p . The other parameters are $\delta = 2\pi \times 1$ MHz, $\Omega = 2\pi \times 0.05$ MHz, $\Delta = 2\pi \times 300$ MHz.

time intervals $\bar{\tau}_{ac(c)}$ shown in Figs. 9(e) and 9(f) to three decimal places and plot the corresponding evolution as shown in Fig. 20. The chiral motion of atomic excitation can still be clearly observed.

As discussed before, the chiral motion can be achieved for triangle structure and a special current with definite direction

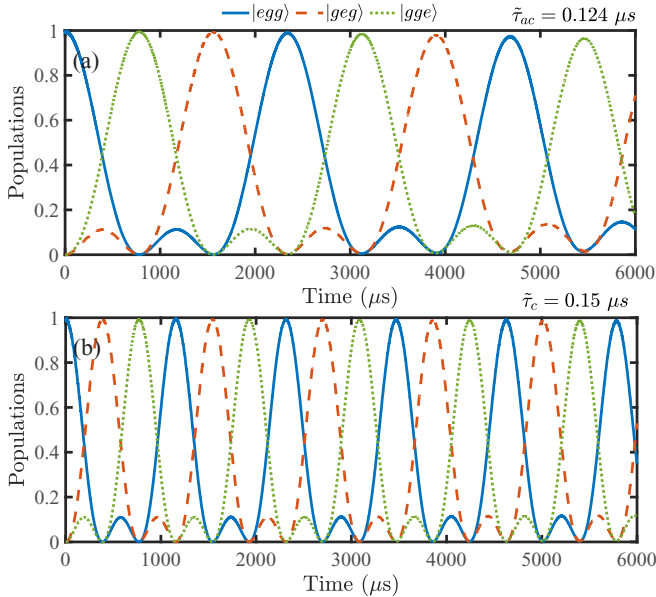


FIG. 20. Populations of ground states as a function of time corresponding to $\Phi_z = \pi/2, -\pi/2$ while the time interval is respectively $0.124 \mu\text{s}$ and $0.15 \mu\text{s}$. The parameters are $\delta = \Omega_p = 2\pi \times 1$ MHz, $\Omega_j = 0.05\Omega_p$, and $\Delta = 2\pi \times 300$ MHz.

can be reached by adjusting time intervals. Thus, a natural question to ask is what will happen for larger lattices under our protocol. For a square geometry, the effective coupling

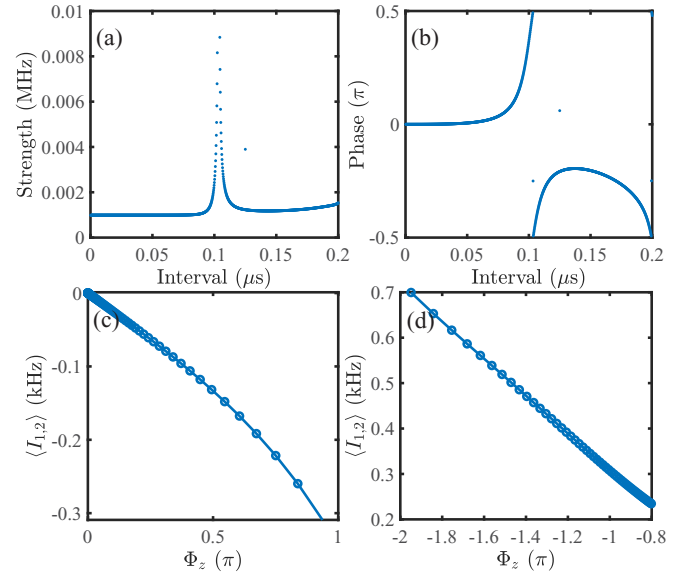


FIG. 21. The chiral motion of atomic excitation under a tight-binding model with $N = 4$ arranged in a square. Panels (a) and (b) respectively show the average value of the effective coupling strength and induced phases under different time intervals. Panels (c) and (d) show the chiral current $\langle I_{1,2} \rangle$ of ground-state governed by the periodical Hamiltonian from the initial state $|egg\rangle$. The corresponding time intervals are $\tau \in [0.001, 0.096] \mu\text{s}$ and $\tau \in [0.13, 0.199] \mu\text{s}$, respectively. The other parameters are $\delta = \Omega_p = 2\pi \times 1$ MHz, $\Omega = 0.05\Omega_p$, and $\Delta = 300\Omega_p$.

strength between the nearest neighbor atoms are basically the same with the periodical Hamiltonian read as

$$H(t) = \begin{cases} H_1, & t \in [0, T/4) \\ H_2, & t \in [T/4, T/2) \\ H_3, & t \in [T/2, 3T/4) \\ H_4, & t \in [3T/4, T), \end{cases} \quad (\text{B16})$$

where

$$H_i = \Omega_i |r_i\rangle \langle g_i| + \sum_{j=1}^4 \Omega_p |r_j\rangle \langle e_j| + \text{H.c.} + \delta |g_j\rangle \langle g_j| + \Delta |e_j\rangle \langle e_j| + \sum_{j<k} \mathcal{U}_{jk} |r_j r_k\rangle \langle r_j r_k|. \quad (\text{B17})$$

Under the same operations, the average value of the effective coupling strength J_{eff} [$J_{\text{eff}} = 1/4(J_{\text{eff}}^1 + J_{\text{eff}}^2 + J_{\text{eff}}^3 + J_{\text{eff}}^4)$] and Φ [$\Phi = 1/4(\Phi_{12} + \Phi_{23} + \Phi_{34} + \Phi_{41})$] according to different time intervals are shown in Figs. 21(a) and 21(b). By tuning the time interval τ , the chiral motion of atomic excitation can be obtained for $\Phi_z \neq 0, \pm 2\pi$. As shown in Figs. 21(c) and 21(d), the ground-state current for bond $1 \rightarrow 2$ has been measured with $\tau \in [0.001, 0.096] \mu\text{s}$ and $\tau \in [0.13, 0.199] \mu\text{s}$, respectively. The other parameters are $\delta = \Omega_p = 2\pi \times 1 \text{ MHz}$, $\Omega = 0.05\Omega_p$, and $\Delta = 300\Omega_p$. It is easy to find that the direction of the ground-state current is related to the sign of Φ_z . However, the chiral motion with each atom reaching the maximum population close to unity in the clockwise or anticlockwise order only exists in the triangle structure with $\Phi_z = \pm\pi/2$.

- [1] S. Bose, Quantum Communication through an Unmodulated Spin Chain, *Phys. Rev. Lett.* **91**, 207901 (2003).
- [2] A. Wójcik, T. Łuczak, P. Kurzyński, A. Grudka, T. Gdala, and M. Bednarska, Unmodulated spin chains as universal quantum wires, *Phys. Rev. A* **72**, 034303 (2005).
- [3] S. Lorenzo, T. J. G. Apollaro, S. Paganelli, G. M. Palma, and F. Plastina, Transfer of arbitrary two-qubit states via a spin chain, *Phys. Rev. A* **91**, 042321 (2015).
- [4] F. A. Mohiyaddin, R. Kalra, A. Laucht, R. Rahman, G. Klimeck, and A. Morello, Transport of spin qubits with donor chains under realistic experimental conditions, *Phys. Rev. B* **94**, 045314 (2016).
- [5] O. Romero-Isart, K. Eckert, and A. Sanpera, Quantum state transfer in spin-1 chains, *Phys. Rev. A* **75**, 050303(R) (2007).
- [6] V. Subrahmanyam, Entanglement dynamics and quantum-state transport in spin chains, *Phys. Rev. A* **69**, 034304 (2004).
- [7] P. Cappellaro, C. Ramanathan, and D. G. Cory, Simulations of Information Transport in Spin Chains, *Phys. Rev. Lett.* **99**, 250506 (2007).
- [8] R. R. Agundez, C. D. Hill, L. C. L. Hollenberg, S. Rogge, and M. Blaauboer, Superadiabatic quantum state transfer in spin chains, *Phys. Rev. A* **95**, 012317 (2017).
- [9] C. Albanese, M. Christandl, N. Datta, and A. Ekert, Mirror Inversion of Quantum States in Linear Registers, *Phys. Rev. Lett.* **93**, 230502 (2004).
- [10] S. Bose, Quantum communication through spin chain dynamics: An introductory overview, *Contemp. Phys.* **48**, 13 (2007).
- [11] M. Christandl, N. Datta, A. Ekert, and A. J. Landahl, Perfect State Transfer in Quantum Spin Networks, *Phys. Rev. Lett.* **92**, 187902 (2004).
- [12] P. Karbach and J. Stolze, Spin chains as perfect quantum state mirrors, *Phys. Rev. A* **72**, 030301(R) (2005).
- [13] D. L. Feder, Perfect Quantum State Transfer with Spinor Bosons on Weighted Graphs, *Phys. Rev. Lett.* **97**, 180502 (2006).
- [14] M.-H. Yung and S. Bose, Perfect state transfer, effective gates, and entanglement generation in engineered bosonic and fermionic networks, *Phys. Rev. A* **71**, 032310 (2005).
- [15] G. Coutinho, L. Vinet, H. Zhan, and A. Zhedanov, Perfect state transfer in a spin chain without mirror symmetry, *J. Phys. A: Math. Theor.* **52**, 455302 (2019).
- [16] L. Vinet and A. Zhedanov, How to construct spin chains with perfect state transfer, *Phys. Rev. A* **85**, 012323 (2012).
- [17] C. Dłaska, B. Vermersch, and P. Zoller, Robust quantum state transfer via topologically protected edge channels in dipolar arrays, *Quantum Sci. Technol.* **2**, 015001 (2017).
- [18] N. Y. Yao, C. R. Laumann, A. V. Gorshkov, H. Weimer, L. Jiang, J. I. Cirac, P. Zoller, and M. D. Lukin, Topologically protected quantum state transfer in a chiral spin liquid, *Nat. Commun.* **4**, 1585 (2013).
- [19] A. D. Greentree, J. H. Cole, A. R. Hamilton, and L. C. L. Hollenberg, Coherent electronic transfer in quantum dot systems using adiabatic passage, *Phys. Rev. B* **70**, 235317 (2004).
- [20] A. D. Greentree and B. Koiller, Dark-state adiabatic passage with spin-one particles, *Phys. Rev. A* **90**, 012319 (2014).
- [21] K. Eckert, O. Romero-Isart, and A. Sanpera, Efficient quantum state transfer in spin chains via adiabatic passage, *New J. Phys.* **9**, 155 (2007).
- [22] F. Mei, G. Chen, L. Tian, S.-L. Zhu, and S. Jia, Robust quantum state transfer via topological edge states in superconducting qubit chains, *Phys. Rev. A* **98**, 012331 (2018).
- [23] F. M. D'Angelis, F. A. Pinheiro, D. Guéry-Odelin, S. Longhi, and F. Impens, Fast and robust quantum state transfer in a topological Su-Schrieffer-Heeger chain with next-to-nearest-neighbor interactions, *Phys. Rev. Research* **2**, 033475 (2020).
- [24] V. Lienhard, S. de Léséleuc, D. Barredo, T. Lahaye, A. Browaeys, M. Schuler, L.-P. Henry, and A. M. Läuchli, Observing the Space- and Time-Dependent Growth of Correlations in Dynamically Tuned Synthetic Ising Models with Antiferromagnetic Interactions, *Phys. Rev. X* **8**, 021070 (2018).
- [25] H. Labuhn, D. Barredo, S. Ravets, S. de Léséleuc, T. Macrì, T. Lahaye, and A. Browaeys, Tunable two-dimensional arrays of single Rydberg atoms for realizing quantum Ising models, *Nature (London)* **534**, 667 (2016).
- [26] A. Browaeys and T. Lahaye, Many-body physics with individually controlled Rydberg atoms, *Nat. Phys.* **16**, 132 (2020).
- [27] H. Bernien, S. Schwartz, A. Keesling, H. Levine, A. Omran, H. Pichler, S. Choi, A. S. Zibrov, M. Endres, M. Greiner, V. Vuletić, and M. D. Lukin, Probing many-body dynamics on a 51-atom quantum simulator, *Nature (London)* **551**, 579 (2017).
- [28] M. Saffman, T. G. Walker, and K. Mølmer, Quantum information with Rydberg atoms, *Rev. Mod. Phys.* **82**, 2313 (2010).

- [29] S. Whitlock, A. W. Glaetzle, and P. Hannaford, Simulating quantum spin models using Rydberg-excited atomic ensembles in magnetic microtrap arrays, *J. Phys. B: At., Mol. Opt. Phys.* **50**, 074001 (2017).
- [30] M. Morgado and S. Whitlock, Quantum simulation and computing with Rydberg-interacting qubits, *AVS Quantum Sci.* **3**, 023501 (2021).
- [31] M. D. Lukin, M. Fleischhauer, R. Cote, L. M. Duan, D. Jaksch, J. I. Cirac, and P. Zoller, Dipole Blockade and Quantum Information Processing in Mesoscopic Atomic Ensembles, *Phys. Rev. Lett.* **87**, 037901 (2001).
- [32] T. Vogt, M. Viteau, A. Chotia, J. Zhao, D. Comparat, and P. Pillet, Electric-Field Induced Dipole Blockade with Rydberg Atoms, *Phys. Rev. Lett.* **99**, 073002 (2007).
- [33] E. Urban, T. A. Johnson, T. Henage, L. Isenhower, D. D. Yavuz, T. G. Walker, and M. Saffman, Observation of Rydberg blockade between two atoms, *Nat. Phys.* **5**, 110 (2009).
- [34] C. Ates, T. Pohl, T. Pattard, and J. M. Rost, Antiblockade in Rydberg Excitation of an Ultracold Lattice Gas, *Phys. Rev. Lett.* **98**, 023002 (2007).
- [35] T. Amthor, C. Giese, C. S. Hofmann, and M. Weidemüller, Evidence of Antiblockade in an Ultracold Rydberg Gas, *Phys. Rev. Lett.* **104**, 013001 (2010).
- [36] M. Marcuzzi, J. Minář, D. Barredo, S. de Léséleuc, H. Labuhn, T. Lahaye, A. Browaeys, E. Levi, and I. Lesanovsky, Facilitation Dynamics and Localization Phenomena in Rydberg Lattice Gases with Position Disorder, *Phys. Rev. Lett.* **118**, 063606 (2017).
- [37] M. Ostmann, M. Marcuzzi, J. P. Garrahan, and I. Lesanovsky, Localization in spin chains with facilitation constraints and disordered interactions, *Phys. Rev. A* **99**, 060101(R) (2019).
- [38] P. P. Mazza, R. Schmidt, and I. Lesanovsky, Vibrational Dressing in Kinetically Constrained Rydberg Spin Systems, *Phys. Rev. Lett.* **125**, 033602 (2020).
- [39] C. H. Greene, A. S. Dickinson, and H. R. Sadeghpour, Creation of Polar and Nonpolar Ultra-Long-Range Rydberg Molecules, *Phys. Rev. Lett.* **85**, 2458 (2000).
- [40] I. C. H. Liu, J. Stanojevic, and J. M. Rost, Ultra-Long-Range Rydberg Trimers with a Repulsive Two-Body Interaction, *Phys. Rev. Lett.* **102**, 173001 (2009).
- [41] D. Barredo, H. Labuhn, S. Ravets, T. Lahaye, A. Browaeys, and C. S. Adams, Coherent Excitation Transfer in a Spin Chain of Three Rydberg Atoms, *Phys. Rev. Lett.* **114**, 113002 (2015).
- [42] D. W. Schönleber, A. Eisfeld, M. Genkin, S. Whitlock, and S. Wüster, Quantum Simulation of Energy Transport with Embedded Rydberg Aggregates, *Phys. Rev. Lett.* **114**, 123005 (2015).
- [43] A. P. Orioli, A. Signoles, H. Wildhagen, G. Günter, J. Berges, S. Whitlock, and M. Weidemüller, Relaxation of an Isolated Dipolar-Interacting Rydberg Quantum Spin System, *Phys. Rev. Lett.* **120**, 063601(R) (2018).
- [44] C. Ates, A. Eisfeld, and J. M. Rost, Motion of Rydberg atoms induced by resonant dipole-dipole interactions, *New J. Phys.* **10**, 045030 (2008).
- [45] H. Schempp, G. Günter, S. Wüster, M. Weidemüller, and S. Whitlock, Correlated Exciton Transport in Rydberg-Dressed-Atom Spin Chains, *Phys. Rev. Lett.* **115**, 093002 (2015).
- [46] F. Letscher and D. Petrosyan, Mobile bound states of Rydberg excitations in a lattice, *Phys. Rev. A* **97**, 043415 (2018).
- [47] F. Yang, S. Yang, and L. You, Quantum Transport of Rydberg Excitons with Synthetic Spin-Exchange Interactions, *Phys. Rev. Lett.* **123**, 063001 (2019).
- [48] G. Günter, H. Schempp, M. Robert-de Saint-Vincent, V. Gavryusev, S. Helmrich, C. S. Hofmann, S. Whitlock, and M. Weidemüller, Observing the dynamics of dipole-mediated energy transport by interaction-enhanced imaging, *Science* **342**, 954 (2013).
- [49] S. Wüster, C. Ates, A. Eisfeld, and J. M. Rost, Excitation transport through Rydberg dressing, *New J. Phys.* **13**, 073044 (2011).
- [50] A. W. Glaetzle, M. Dalmonte, R. Nath, C. Gross, I. Bloch, and P. Zoller, Designing Frustrated Quantum Magnets with Laser-Dressed Rydberg Atoms, *Phys. Rev. Lett.* **114**, 173002 (2015).
- [51] R. M. W. van Bijnen and T. Pohl, Quantum Magnetism and Topological Ordering Via Rydberg Dressing Near Förster Resonances, *Phys. Rev. Lett.* **114**, 243002 (2015).
- [52] P. Jurcevic, B. P. Lanyon, P. Hauke, C. Hempel, P. Zoller, R. Blatt, and C. F. Roos, Quasiparticle engineering and entanglement propagation in a quantum many-body system, *Nature (London)* **511**, 202 (2014).
- [53] D. X. Li and X. Q. Shao, Unconventional Rydberg pumping and applications in quantum information processing, *Phys. Rev. A* **98**, 062338 (2018).
- [54] X.-Q. Shao, Selective Rydberg pumping via strong dipole blockade, *Phys. Rev. A* **102**, 053118 (2020).
- [55] O. V. Marchukov, A. G. Volosniev, M. Valiente, D. Petrosyan, and N. T. Zinner, Quantum spin transistor with a Heisenberg spin chain, *Nat. Commun.* **7**, 13070 (2016).
- [56] A. Smith, M. S. Kim, F. Pollmann, and J. Knolle, Simulating quantum many-body dynamics on a current digital quantum computer, *npj Quantum Inf.* **5**, 106 (2019).
- [57] P. N. Jepsen, J. Amato-Grill, I. Dimitrova, W. W. Ho, E. Demler, and W. Ketterle, Spin transport in a tunable Heisenberg model realized with ultracold atoms, *Nature (London)* **588**, 403 (2020).
- [58] W. P. Su, J. R. Schrieffer, and A. J. Heeger, Solitons in Polyacetylene, *Phys. Rev. Lett.* **42**, 1698 (1979).
- [59] J. Zak, Berry's Phase for Energy Bands in Solids, *Phys. Rev. Lett.* **62**, 2747 (1989).
- [60] J. K. Asbóth, L. Oroszlány, and A. Pályi, *A Short Course on Topological Insulators* (Lecture Notes in Physics, Switzerland, 2016), Vol. 919.
- [61] P. Roushan, C. Neill, A. Megrant, Y. Chen, R. Babbush, R. Barends, B. Campbell, Z. Chen, B. Chiaro, A. Dunsworth, A. Fowler, E. Jeffrey, J. Kelly, E. Lucero, J. Mutus, P. J. J. O'Malley, M. Neeley, C. Quintana, D. Sank, A. Vainsencher *et al.*, Chiral ground-state currents of interacting photons in a synthetic magnetic field, *Nat. Phys.* **13**, 146 (2017).
- [62] V. Lienhard, P. Scholl, S. Weber, D. Barredo, S. de Léséleuc, R. Bai, N. Lang, M. Fleischhauer, H. P. Büchler, T. Lahaye, and A. Browaeys, Realization of a Density-Dependent Peierls Phase in a Synthetic, Spin-Orbit Coupled Rydberg System, *Phys. Rev. X* **10**, 021031 (2020).
- [63] S. H. Cantu, A. V. Venkatramani, W. Xu, L. Zhou, B. Jelenković, M. D. Lukin, and V. Vuletić, Repulsive photons in a quantum nonlinear medium, *Nat. Phys.* **16**, 921 (2020).
- [64] Y. O. Dudin, L. Li, F. Bariani, and A. Kuzmich, Observation of coherent many-body Rabi oscillations, *Nat. Phys.* **8**, 790 (2012).

- [65] N. Šibalić, J. D. Pritchard, C. S. Adams, and K. J. Weatherill, Arc: An open-source library for calculating properties of alkali Rydberg atoms, *Comput. Phys. Commun.* **220**, 319 (2017).
- [66] F. Reiter and A. S. Sørensen, Effective operator formalism for open quantum systems, *Phys. Rev. A* **85**, 032111 (2012).
- [67] M. J. Kastoryano, F. Reiter, and A. S. Sørensen, Dissipative Preparation of Entanglement in Optical Cavities, *Phys. Rev. Lett.* **106**, 090502 (2011).
- [68] M. Saffman, I. I. Beterov, A. Dalal, E. J. Pérez, and B. C. Sanders, Symmetric Rydberg controlled- z gates with adiabatic pulses, *Phys. Rev. A* **101**, 062309 (2020).
- [69] J. D. Franson, B. C. Jacobs, and T. B. Pittman, Quantum computing using single photons and the Zeno effect, *Phys. Rev. A* **70**, 062302 (2004).
- [70] J. R. Petta, A. C. Jonson, J. M. Taylor, E. A. Laird, A. Yacoby, M. D. Lukin, C. M. Marcus, M. P. Hanson, and A. C. Gossard, Coherent manipulation of coupled electron spins in semiconductor quantum dots, *Science* **309**, 2180 (2005).
- [71] M. Anderlini, P. J. Lee, B. L. Brown, J. Sebby-Strabley, W. D. Phillips, and J. V. Porto, Controlled exchange interaction between pairs of neutral atoms in an optical lattice, *Nature (London)* **448**, 452 (2007).
- [72] S. Zhang, X.-Q. Shao, L. Chen, Y.-F. Zhao, and K.-H. Yeon, Robust $\sqrt{\text{SWAP}}$ gate on nitrogen-vacancy centres via quantum Zeno dynamics, *J. Phys. B: At., Mol. Opt. Phys.* **44**, 075505 (2011).
- [73] X.-Q. Shao, J.-B. You, T.-Y. Zheng, and C. H. Oh, Long-range universal quantum computation in a large-size coupled cavity array independent of cavity number, *Laser Phys. Lett.* **11**, 105203 (2014).
- [74] K. Mochizuki, N. Hatano, J. Feinberg, and H. Obuse, Statistical properties of eigenvalues of the non-Hermitian Su-Schrieffer-Heeger model with random hopping terms, *Phys. Rev. E* **102**, 012101 (2020).
- [75] B. Ostahie and A. Aldea, Spectral analysis, chiral disorder and topological edge states manifestation in open non-Hermitian Su-Schrieffer-Heeger chains, *Phys. Lett. A* **387**, 127030 (2021).
- [76] H. Jiang, R. Lü, and S. Chen, Topological invariants, zero mode edge states and finite size effect for a generalized non-reciprocal Su-Schrieffer-Heeger model, *Eur. Phys. J. B* **93**, 125 (2020).
- [77] S. de Léséleuc, V. Lienhard, P. Scholl, D. Barredo, S. Weber, N. Lang, H. P. Büchler, T. Lahaye, and A. Browaeys, Observation of a symmetry-protected topological phase of interacting bosons with Rydberg atoms, *Science* **365**, 775 (2019).
- [78] M. Bukov, L. D'Alessio, and A. Polkovnikov, Universal high-frequency behavior of periodically driven systems: From dynamical stabilization to Floquet engineering, *Adv. Phys.* **64**, 139 (2015).
- [79] S. Denisov, L. Morales-Molina, S. Flach, and P. Hänggi, Periodically driven quantum ratchets: Symmetries and resonances, *Phys. Rev. A* **75**, 063424 (2007).
- [80] Z. Ovadyahu, Suppression of Inelastic Electron-Electron Scattering in Anderson Insulators, *Phys. Rev. Lett.* **108**, 156602 (2012).
- [81] S. Iwai, M. Ono, A. Maeda, H. Matsuzaki, H. Kishida, H. Okamoto, and Y. Tokura, Ultrafast Optical Switching to a Metallic State by Photoinduced Mott Transition in a Halogen-Bridged Nickel-Chain Compound, *Phys. Rev. Lett.* **91**, 057401 (2003).
- [82] S. Kaiser, C. R. Hunt, D. Nicoletti, W. Hu, I. Gierz, H. Y. Liu, M. Le Tacon, T. Loew, D. Haug, B. Keimer, and A. Cavalleri, Optically induced coherent transport far above T_c in underdoped $\text{YBa}_2\text{Cu}_3\text{O}_{6+\delta}$, *Phys. Rev. B* **89**, 184516 (2014).
- [83] G. Goldstein, C. Aron, and C. Chamon, Photoinduced superconductivity in semiconductors, *Phys. Rev. B* **91**, 054517 (2015).
- [84] M. O. Scully and M. S. Zubairy, *Quantum Optics* (Quantum Optics, Cambridge, 2000).
- [85] Simon, Barry, Reed, and Michael, *Methods of Modern Mathematical Physics, I: Functional Analysis* (Academic Press, New York, London, 1980), Vol. 14, pp. 9–66.
- [86] K.-J. Engel and R. Nagel, One-parameter semigroups for linear evolution equations, *Semigroup Forum* **63**, 278 (2001).
- [87] M. Keck, D. Rossini, and R. Fazio, Persistent currents by reservoir engineering, *Phys. Rev. A* **98**, 053812 (2018).
- [88] I. Vasić, A. Petrescu, K. Le Hur, and W. Hofstetter, Chiral bosonic phases on the Haldane honeycomb lattice, *Phys. Rev. B* **91**, 094502 (2015).
- [89] K. Plekhanov, I. Vasić, A. Petrescu, R. Nirwan, G. Roux, W. Hofstetter, and K. Le Hur, Emergent Chiral Spin State in the Mott Phase of a Bosonic Kane-Mele-Hubbard Model, *Phys. Rev. Lett.* **120**, 157201 (2018).